Astronomy & Astrophysics manuscript no. output
October 29, 2021

Tight asteroseismic constraints on age, core-mass, and differential rotation in TESS β Cep star HD192575.

S. Burssens[1], D. M. Bowman[1], M. Michielsen[1], S. Simón-Díaz[2,3], G. Banyard[1], J. S. G. Mombarg[1], and C. Aerts[1,4,5]

[1] Institute of Astronomy, KU Leuven, Celestijnenlaan 200D, 3001 Leuven, Belgium
e-mail: siemen.burssens@kuleuven.be
[2] Instituto de Astrofísica de Canarias, 38200 La Laguna, Tenerife, Spain
[3] Departamento de Astrofísica, Universidad de La Laguna, 38205 La Laguna, Tenerife, Spain
[4] Department of Astrophysics, IMAPP, Radboud University Nijmegen, 6500 GL Nijmegen, The Netherlands
[5] Max Planck Institute for Astronomy, Königstuhl 17, 69117 Heidelberg, Germany

Received xxx; accepted xxx

ABSTRACT

Context. Uncertainties associated with the physics of stellar interiors make it difficult to determine the length of the main-sequence for massive stars. The Transiting Exoplanet Survey Satellite (TESS) mission is the first space telescope to observe large numbers of pulsating massive stars, opening up the avenue to ensemble asteroseismic modelling of supernova progenitors. For the first time this allows us to derive precise constraints on the mass, age, and internal physics, such as rotation, core-boundary mixing and envelope mixing over a large range in mass and evolutionary stage.
Aims. We aim to precisely measure the mass, age and constrain the core-boundary mixing of the newly-discovered high-mass β Cep star, HD 192575, using HERMES spectroscopy and TESS photometry.
Methods. We perform spectroscopic and photometric analyses to derive the atmospheric parameters and pulsation frequencies of HD 192575. We use this information to select optimal stellar models based on the Mahalanobis distance from a grid of pulsation models constructed using the MESA stellar evolution and the GYRE pulsation codes.
Results. We derive an effective temperature $T_{\rm eff} = 25200^{+400}_{-400}$ K, a surface gravity of $\log g = 3.74^{+0.05}_{-0.05}$ dex and a projected surface rotation velocity of $v \sin i = 27^{+6}_{-8}$ km s^{-1}. The TESS photometry reveals a rich frequency spectrum containing several rotationally-split frequency multiplets. Through forward modelling we derive a mass $M_\star = 13.0^{+3.5}_{-0.5}$ M$_\odot$ and a core hydrogen content $X_{\rm c} = 0.156^{+0.050}_{-0.055}$ which corresponds to an age of $14.1^{+1.7}_{-4.6}$ Myr. By estimating the core-boundary mixing $f_{\rm CBM}$ we infer a convective core mass of $M_{\rm cc} = 3.0^{+1.3}_{-0.3}$ M$_\odot$. We measure differential rotation and estimate the near core to be rotating 8.3 times faster than the envelope. From rotational modulation we find the surface rotation frequency of the star to be $f_{\rm rot} = 0.19704(4)$ d^{-1}, which in combination with the spectroscopic $v \sin i$ and model radius is used to calculate a surface equatorial velocity $v_{\rm eq} = 97 \pm 10$ km s^{-1} and an inclination $i = 16 \pm 6^\circ$.

1. Introduction

Massive stars (> 8 M$_\odot$) are crucial contributors to the chemical and energetic evolution of galaxies. While their general evolution is well established (Kippenhahn et al. 2012; Langer 2012), uncertainties in the 1D physical prescriptions of stellar models can lead to a plethora of internal processes leading to different evolutionary paths (e.g. Martins et al. 2017) and therefore chemical yields left behind after the inevitable supernova explosion. This includes the treatment of interior rotation (Hirschi et al. 2004; Maeder 2009), convection (Davis et al. 2019; Kaiser et al. 2020), chemical networks and atomic diffusion (Farmer et al. 2016; Salaris & Cassisi 2017), magnetic fields (Keszthelyi et al. 2019), and mass loss rates (Georgy et al. 2011; Keszthelyi et al. 2017). At present, several complementary strategies to tackle these uncertain processes are being pursued, including multidimensional simulations of the dynamical stellar interior (Meakin & Arnett 2007; Gilet et al. 2013; Cristini et al. 2017; Horst et al. 2020; Higl et al. 2021; Horst et al. 2021), comparison of stellar parameters and abundances obtained spectroscopically for large samples of massive stars with stellar evolution predictions (Hunter et al. 2008; Ramírez-Agudelo et al. 2013; Simón-Díaz & Herrero 2014; McEvoy et al. 2015; Simón-Díaz et al. 2017; Dufton et al. 2018), and asteroseismic modelling of pulsation mode frequencies using long time base photometry.

The high-mass β Cephei stars (or β Cep) are particularly promising for asteroseismic sounding in the massive star regime (Bowman 2020). These stars are between approximately 8 and 25 M$_\odot$ tend to have frequency spectra composed of pressure and gravity modes which under certain circumstances facilitate mode identification and allow for asteroseismic modelling (Stankov & Handler 2005; Aerts et al. 2011). A handful of β Cep stars have been investigated in this way, providing valuable clues to their interior properties. These studies were able to gauge individual levels of convective-boundary mixing, such as HD 129929 (Aerts et al. 2003; Dupret et al. 2004), β CMa (Mazumdar et al. 2006), HD 46202 (Briquet et al. 2011), HD 180642 (Aerts et al. 2011), V2052 Oph (Briquet et al. 2012), and θ Oph (Walczak et al. 2019). Moreover, the detection of rotationally-split pulsation modes has allowed for the detection of differential rotation in several stars, including ν Eridani (Pamyatnykh et al. 2004; Dziembowski & Pamyatnykh 2008), and HD 129929 (Dupret et al. 2004) and anchors the study of angular momentum transport in massive main sequence stars. Studies of mode excitation on the other hand have hinted at shortcomings in standard-opacity models and the inferred location of the instability re-

Table 1. Observational parameters of HD 192575.

Parameter	HD 192575
α_{2000}	$20^h10^m56.911^s$
δ_{2000}	$+68°16'19.971''$
l	101.43°
b	+18.15°
m_V[1] [mag]	6.840
m_{TESS} [mag]	6.7108
Gaia distance[2] [pc]	633 ± 7
Spectral type[3]	B0.5 V

Notes: 1) Oja (1991), 2) Bailer-Jones et al. (2021), 3) Hohle et al. (2010).

gions in the HR diagram (Pamyatnykh et al. 2004; Daszyńska-Daszkiewicz et al. 2017; Walczak et al. 2019). We refer to Bowman 2020 for a recent overview of the state of the art for massive star asteroseismology.

The lack of long time-base photometry has hindered the investigation of β Cep stars on large scales. Often single star observations by space missions such as MOST (Walker et al. 2003) CoRoT (Auvergne et al. 2009), and BRITE (Weiss et al. 2014, 2021), or long spectroscopic campaigns (e.g. Aerts et al. 2004; Jerzykiewicz et al. 2005; Handler et al. 2005) were the only suitable data sets available. This lack of time series data for massive stars is now remedied by the TESS space mission (Ricker et al. 2015) which shows excellent prospects for the study of β Cep stars (Handler et al. 2019; Pedersen et al. 2019; Burssens et al. 2020; Southworth et al. 2020, 2021). In this paper we perform detailed asteroseismic modelling of the interior physics of the newly-discovered β Cep star HD 192575 by combining high-resolution spectroscopy and high-precision TESS space photometry, making it a new and valuable benchmark star for future studies.

2. Spectroscopy

2.1. Prior literature

HD 192575 is a northern early-type star (B0.5 V, Hill & Lynas-Gray 1977; Hohle et al. 2010) found at intermediate galactic latitude (l = +18.15°, Maitre 1965; Guetter 1968; Hill & Lynas-Gray 1977; Gaia Collaboration et al. 2018), and is located in the TESS northern continuous viewing zone (TESS-NCVZ). Before the TESS observations, HD 192575 had gone largely unnoticed with only a handful appearances in large-scale surveys and no dedicated studies. We summarise its global observational parameters in Table 1. The parallax of HD 192575 was measured in Gaia-DR2, π = 1.47 ± 0.03, which corresponds to a distance of d = 680 ± 12 parsec (Gaia Collaboration et al. 2018; Bailer-Jones et al. 2018) from Earth. These values were updated recently in Gaia-EDR3, π = 1.56 ± 0.02, and d = 633 ± 7 parsec (Gaia Collaboration et al. 2021; Bailer-Jones et al. 2021). Hohle et al. (2010) estimated a mass of 12.53 ± 0.73 $M_\odot$ using an effective temperature ($T_{\rm eff}$ ≈ 27700 K) and luminosity ($\log(L/L_\odot)$ = 4.26 dex) derived from multi-colour 2MASS and HIPPARCOS photometry.

Table 2. Overview of the available spectra used in this work.

HJD (d)	Exposure time (s)	S/N (5300Å)	RV (km s^{-1})
2458672.672427	180	96	−36.95 ± 0.09
2458684.485646	177	102	−38.28 ± 0.09
2459095.409159	700	164	−38.87 ± 0.04
2459096.453308	700	165	−36.60 ± 0.04

2.2. Observed spectra

We obtained two spectra of HD 192575, in July 2019 with the high-resolution HERMES spectrograph (R ≈ 85000) mounted on the 1.2m Mercator Telescope in La Palma, Spain (Raskin et al. 2011) as part of a preliminary spectroscopic survey of the TESS Northern-CVZ OB stars. After viewing the TESS data of HD 192575 we obtained two additional spectra in September 2020. The observation log is given in Table 2. The raw spectra were reduced using the HERMES data reduction pipeline (HERMES-DRS, v.7.0), which includes bias correction, flat-fielding, wavelength calibration, cosmic removal and correction for barycentric motion (Raskin et al. 2011).

We normalised all spectra manually using spline fits and calculated radial velocities (RV) using the method given in Banyard et al. (2021). Lorentzian profiles were fit to five He I lines (He I λ4009, 4026, 5015, 5876, 6678Å) and the Si III λ4552Å line. For each spectral line, the profile of the Lorentzian was fixed through all epochs and all the lines in one epoch are forced to have the same RV shift. The derived RVs are given in Table 2. They show no significant variations and agree with previous measurements (Wilson 1953). Since the spectra sample several days and then several days a year later we rule out short/intermediate period binarity ($P \lesssim 1000$ d).

We searched the spectra for noticeable features, including line-profile variations (indicating non-radial pulsations) or lines in emission (indicating the presence of a strong wind). Early B-type stars with β Cep type pulsations are known to have line-profile variations (LPVs) of the order of hours, induced by photospheric velocity fields, in their spectra (Aerts & De Cat 2003). The Si III triplet (Si III λ4552, 4567, 4574 Å) in particular, is commonly used to study the imprint of these pulsations due to their strength in this temperature regime. We show the line profiles of the Si III triplet of HD 192575 for the different epochs in Fig. 1. Si III λ4552 Å in particular shows asymmetric variations, hinting at the presence of non-radial pulsations. No lines were found in emission.

2.3. Atmospheric parameters

The mass regime of β Cep stars is where non-local thermodynamic equilibrium effects (non-LTE, or NLTE) start to become important for the determination of atmospheric parameters. It is therefore worthwhile to test whether LTE atmosphere models are sufficient to derive the atmospheric parameters of HD 192575. In a first instance we used the Grid Search in Stellar Parameters code (GSSP; Tkachenko 2015) which employs the SynthV radiative transfer code (Tsymbal 1996) coupled to LTE atmosphere models from Castelli & Kurucz (2003). In a second instance we

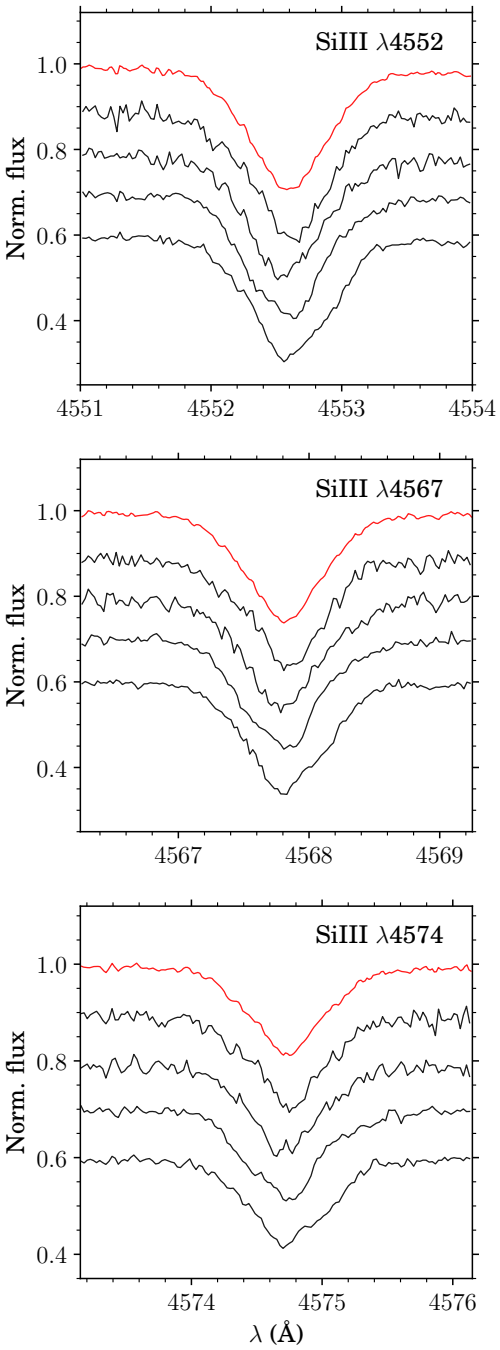

Fig. 1. Line profiles of the Si III triplet lines, which are sensitive to non-radial pulsations in the photosphere of a β Cep star. The observed line profiles are shown in black and a mean profile is shown in red. The lines of the different spectra are shifted vertically by 0.1, and plotted in order of Table 2.

followed a similar analysis strategy as described in Simón-Díaz (2010), which is based on a combined curve-of-growth analysis of Si III-IV lines and a profile fitting of the Balmer lines, and which employs an extensive grid of NLTE atmosphere models computed with the FASTWIND code (Santolaya-Rey et al. 1997; Puls et al. 2005; Rivero González et al. 2012; Carneiro et al. 2016; Sundqvist & Puls 2018; Puls et al. 2020).

2.3.1. LTE - GSSP

We used GSSP to estimate the effective temperature $T_{\rm eff}$, surface gravity $\log g$, the metallicity [M/H], and the line-broadening parameters including the projected surface velocity ($v \sin i$), the macroturbulent broadening ($v_{\rm macro}$), and the microturbulent broadening (ξ_t). The GSSP fitting mode allows the user to fit large wavelength ranges or separate lines, using a χ^2 estimator to determine the goodness of fit.

We used the Fourier method (Carroll 1933; Gray 2005; Simón-Díaz et al. 2006; Simón-Díaz & Herrero 2014; Aerts et al. 2014) on the four separate spectra to determine a first estimate of the projected rotational velocity which we find to be $v \sin i \sim 27$ km s^{-1}, making it a relatively slow rotator. We proceeded by estimating $T_{\rm eff}$ using the Si III/IV ionisation balance which are typically available in the β Cep temperature regime. The surface gravity was estimated using the Balmer lines (Hβ, Hδ and Hγ), and the line-broadening parameters $v \sin i$, ξ_t and $v_{\rm macro}$ using several metal lines (Si III λ4552, 4567, 4574, 4819, 4829 Å and C II λ5133, 5143, 5151, 6578, 6582Å). The procedure of fitting the ionisation balance for $T_{\rm eff}$ and Balmer lines for $\log g$, and metal lines for all broadening parameters was repeated until the parameters stop varying. The final parameters are given in Table 3. To test the robustness of our results we also used normalisations from two different authors which lead to the same final parameters within their uncertainties. The derived $T_{\rm eff}$ and $\log g$ of HD 192575 place it within the predicted β Cep instability region (Pamyatnykh 1999; Walczak et al. 2015).

2.3.2. NLTE - FASTWIND

In a next step we used the `iacob-broad` tool (Simón-Díaz & Herrero 2014) and followed the analysis strategy of Simón-Díaz (2010) to obtain estimates of the line-broadening and atmospheric parameters, respectively. In particular, $T_{\rm eff}$, $\log g$ and ξ_t resulted from a quantitative spectroscopic analysis based on a grid of FASTWIND NLTE atmosphere models computed at solar metallicity. The assumption of solar metallicity is valid given the lack of significant metal enrichment/depletion found in the previous section using GSSP. The final results are given in Table 3. Again the results indicate that the star falls within the typical β Cep instability regime (Pamyatnykh 1999; Walczak et al. 2015).

The effective temperature $T_{\rm eff}$ and the line-broadening parameters $v \sin i$ and $v_{\rm macro}$ agree within their uncertainties with the results obtained with GSSP, but a discrepancy of 0.2 dex is found for $\log g$. This discrepancy was found to be independent of the normalisation procedure of different authors and the use of separate or merged spectra. We therefore attribute it to the differences in thermodynamic equilibrium assumptions between the codes. Indeed, we found it difficult to fit the line cores of the Balmer lines with GSSP (see Fig 2), which is a known effect in this temperature regime and can lead to an overestimation of the surface gravity (Nieva & Przybilla 2007). Therefore, we consider the FASTWIND results to be more reliable and used these in the remainder of the analysis. On the other hand, since $\log g$ is more sensitive to the data quality and normalisation, it is noteworthy that GSSP provides reliable estimates for the effective temperature and metallicity of β Cep stars.

3. Photometry

HD 192575 was observed by TESS in short-cadence mode (i.e. 2 min) between sectors 15 and 26, with the exception of sectors

Table 3. Atmospheric and line-broadening parameters of HD 192575 derived using GSSP and FASTWIND.

Parameter	Value (GSSP)	Value (FASTWIND)	Diagnostic lines
M/H [dex]	$-0.02^{+0.04}_{-0.04}$	NA	4000 – 5700Å
$T_{\rm eff}$ [K]	25600^{+400}_{-400}	25200^{+400}_{-400}	Si lines
$\log g$ [dex]	$3.95^{+0.07}_{-0.07}$	$3.74^{+0.05}_{-0.05}$	Balmer lines
ξ_t [km s^{-1}]	$8.8^{+0.8}_{-0.8}$	5.6^{+1}_{-1}	Metal lines
$v \sin i$ [km s^{-1}]	26^{+2}_{-2}	27^{+6}_{-8}	Metal lines
$v_{\rm macro}$ [km s^{-1}]	27^{+3}_{-3}	31^{+9}_{-8}	Metal lines

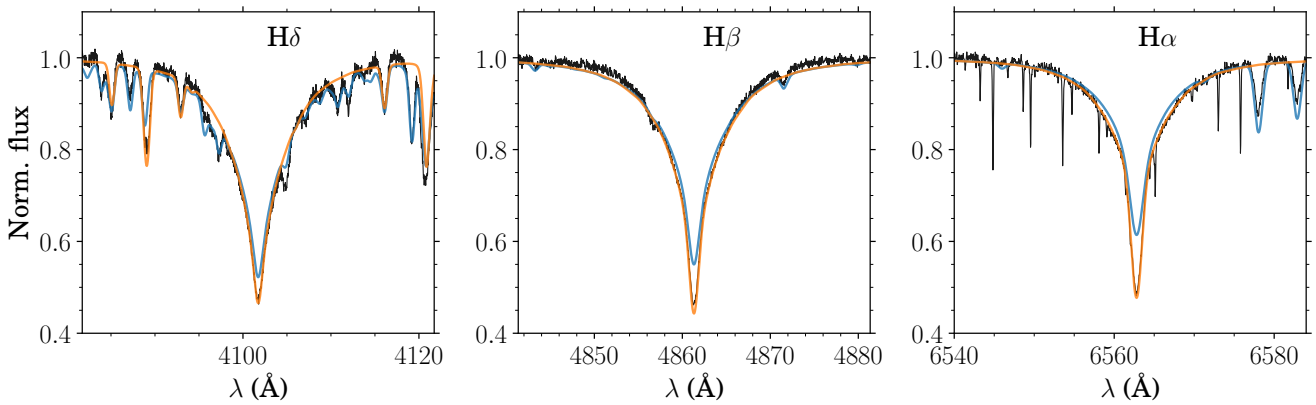

Fig. 2. The fitted Balmer lines (Hδ, Hβ, Hα) used as surface gravity diagnostics. The observed spectrum is given in black, while the GSSP and FASTWIND fits of the best models are given in blue and orange, respectively.

20 and 23. We performed a first inspection of the short cadence TESS data using the `lightkurve` software package (Lightkurve Collaboration et al. 2018) in order to rule out any large aperture mask variations or significant light contamination by other stars. A sector-by-sector analysis showed no significant variations of the aperture mask, and the star is seemingly isolated based on the overlay of Gaia measurements (Gaia Collaboration et al. 2018) except for a few dim sources ($\Delta G > 8$ mag), see Appendix A.

3.1. Light curve extraction and reduction

We extracted the TESS 2-min short cadence from the Mikulski Archive for Space Telescopes (MAST[1]) directly in light curve format. We extracted two light curves, the light curve extracted using simple aperture photometry (referred to as SAP), and the pre-conditioned light curve (PDCSAP, Pre-search Data Conditioning Simple Aperture Photometry). The PDCSAP light curve goes through an additional pipeline which removes systematics common to all stars on the same CCD (Jenkins et al. 2016). However, thorough checks are needed since the pipeline is optimised for the detection of exoplanets around low mass stars and may not be optimal to study stellar variability.

We compare both light curves in Fig 3, in which the PDCSAP and SAP light curves are shown for different time-scales of interest. HD 192575 exhibits multi-periodic variability on the order of several hours up to several days. In the top panel of Fig. 3 we plot the full light curves spanning 1 yr which shows that the overall morphology of both versions is similar. In the middle panel we plot a cut-out of Sectors 17-18 where the largest differences between the PDCSAP and SAP light curves are evident. The SAP light curve shows a slight upwards trend towards BJD-2458789, which decreases around BJD-2458792. The TESS pipeline removes this trend which is instrumental in origin. However, the PDCSAP pipeline also systematically removes chunks of data at the end of sectors (e.g. between BJD-2458801 and BJD-2458803). We therefore opted to use the SAP version for the improved duty cycle (75.7% vs. 68.3%), and applied our own corrections using low-degree polynomial fits where needed (grey data points in Fig. 3). This does not affect the short-period pulsations (see lower panel of Fig 3). Our detrended version of the SAP light curve has a time base of ΔT = 323.77 d and a frequency resolution $f_{\rm res} = 1/\Delta{\rm T} = 0.0031$ d^{-1}.

3.2. Frequency analysis

Our frequency analysis consisted of two stages, extraction of the frequencies, and subsequent filtering by excluding any frequencies not suitable for asteroseismic modelling. In the first stage we used our detrended SAP light curve and extracted the frequencies using *iterative pre-whitening* (Degroote et al. 2009; Pápics et al. 2012)[2]. At each step we identified the frequency with the highest signal-to-noise ratio (S/N), using a Lomb-Scargle (LS,

[1] https://archive.stsci.edu/

[2] https://github.com/IvS-KULeuven/IvSPythonRepository

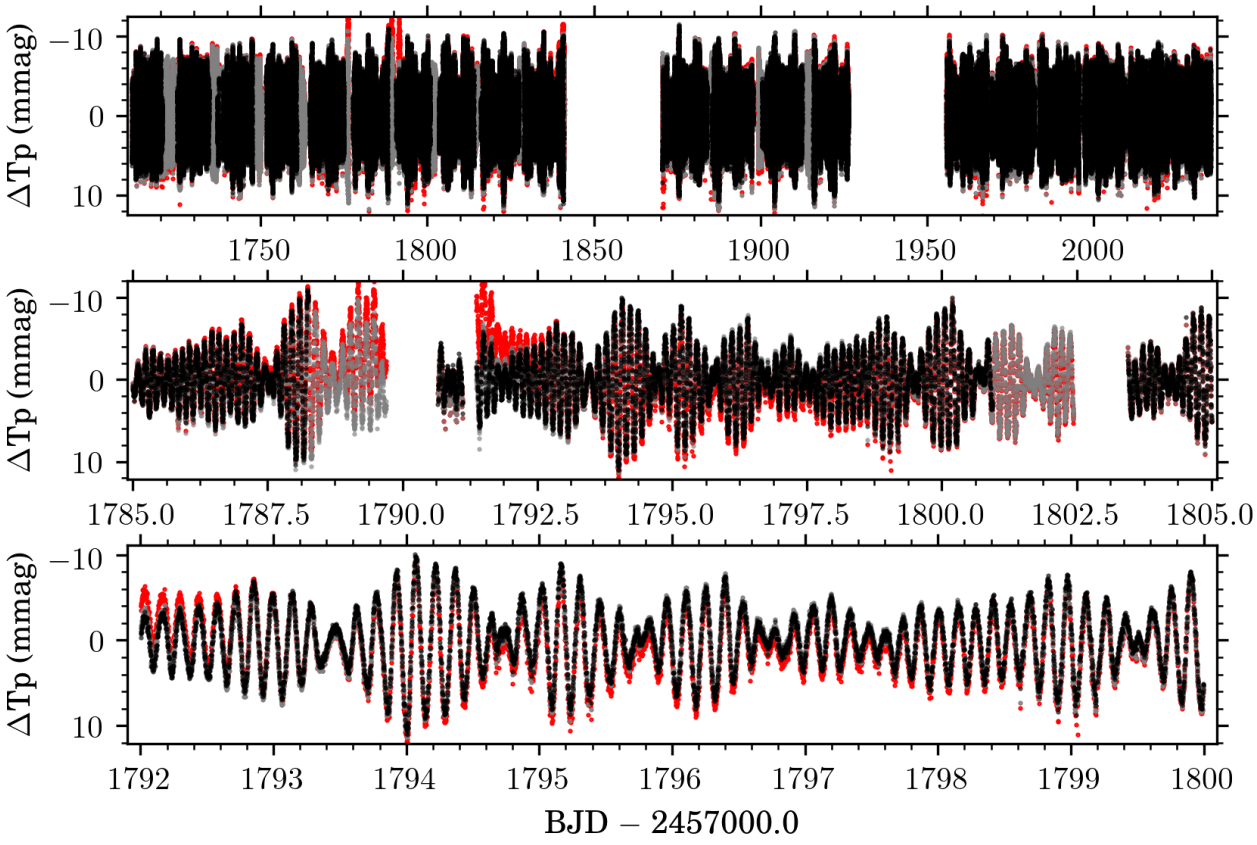

Fig. 3. TESS light curves obtained for HD 192575 shown on different time-scales. From top to bottom: the full year, a month, and a week. The three light curves are stacked in the following order SAP (red), SAP detrended (grey), PDC (black).

Lomb 1976; Scargle 1982) periodogram of the light curve. The resulting frequency was used to fit a sine wave model to the time-series, from which we obtain amplitude and phase values. This model was substracted from the time-series and the residual time-series was used in a next iteration. We repeated the iterations until the S/N of a frequency in the LS-periodogram is below five, following Baran et al. (2015) and Baran & Koen (2021). The S/N is calculated in a window of 1 d^{-1} around the frequency, thus allowing us to avoid over-interpretation of the TESS data (we refer to Appendix A in Burssens et al. 2020 for more details). The frequency extraction yielded a total of 102 frequencies between 0.09 and 22 d^{-1}.

This frequency list was subject to a first interpretation in which we focused on unresolved frequencies and alias frequencies (both a result of the undersampling of real frequencies, see Bowman 2017). Unresolved frequencies were identified by verifying whether pairs of frequencies (f_n, f_m) satisfy the Loumos & Deeming criterion, $|f_n - f_m| > 2.5 f_{\rm res}$, with $f_{\rm res}$ the frequency resolution defined above (Loumos & Deeming 1978). Frequency pairs not satisfying this criterion are difficult to distinguish from artefacts introduced by the convolution of the real intrinsic frequency spectrum of the star with the spectral window caused by the observing times. When such a pair was identified the lower amplitude frequency was discarded. Alias frequencies were not detected which is not surprising given the TESS 2-min short cadence. This procedure yielded 96 significant and well-resolved frequencies.

The next step involved identifying harmonics and combination frequencies of the form $f_i = m \cdot f_j + n \cdot f_k$ where f_i is the combination frequency, f_j, f_k the 'parent' frequencies, and $n, m \in \mathbb{Z}$. These combination frequencies are common in early-type stars with heat-driven pulsations (Degroote et al. 2009; Bowman 2017; Pápics et al. 2017; Pedersen et al. 2021). We identified a combination or harmonic frequency f_i if $|f_i - (m \cdot f_j + n \cdot f_k)| < 2.5 f_{\rm res}$, requiring that the amplitude of the combination frequency is less than that of the parent frequencies. In addition we limited ourselves to $n, m \in [\pm 1, \pm 2, \pm 3]$ and only considered the ten highest amplitude frequencies as parent frequencies, in order to avoid chance matches which may occur in dense frequency spectra (see Van Beeck et al. 2021). This yielded 12 combination frequencies and 5 harmonics (including two of the dominant frequency). These frequencies were removed as they are not used as independent pulsation mode frequencies in our forward asteroseismic modelling.

The resulting frequency list contained 79 independent pulsation mode frequencies. In a final step we performed a multi-frequency non-linear least-squares fit to the light curve in order to optimise the remaining frequencies, amplitudes and phases, which was shown to be important step in forward seismic modelling by Bowman & Michielsen (2021). The final list of independent pulsation mode frequencies is provided in Appendix B.

3.3. Frequency interpretation and detection of multiplets

Pulsation modes are characterised by their angular degree ℓ, azimuthal order m, and radial order $n_{\rm pg}$. Historically, β Cep stars are known to pulsate in low radial order, low-angular degree

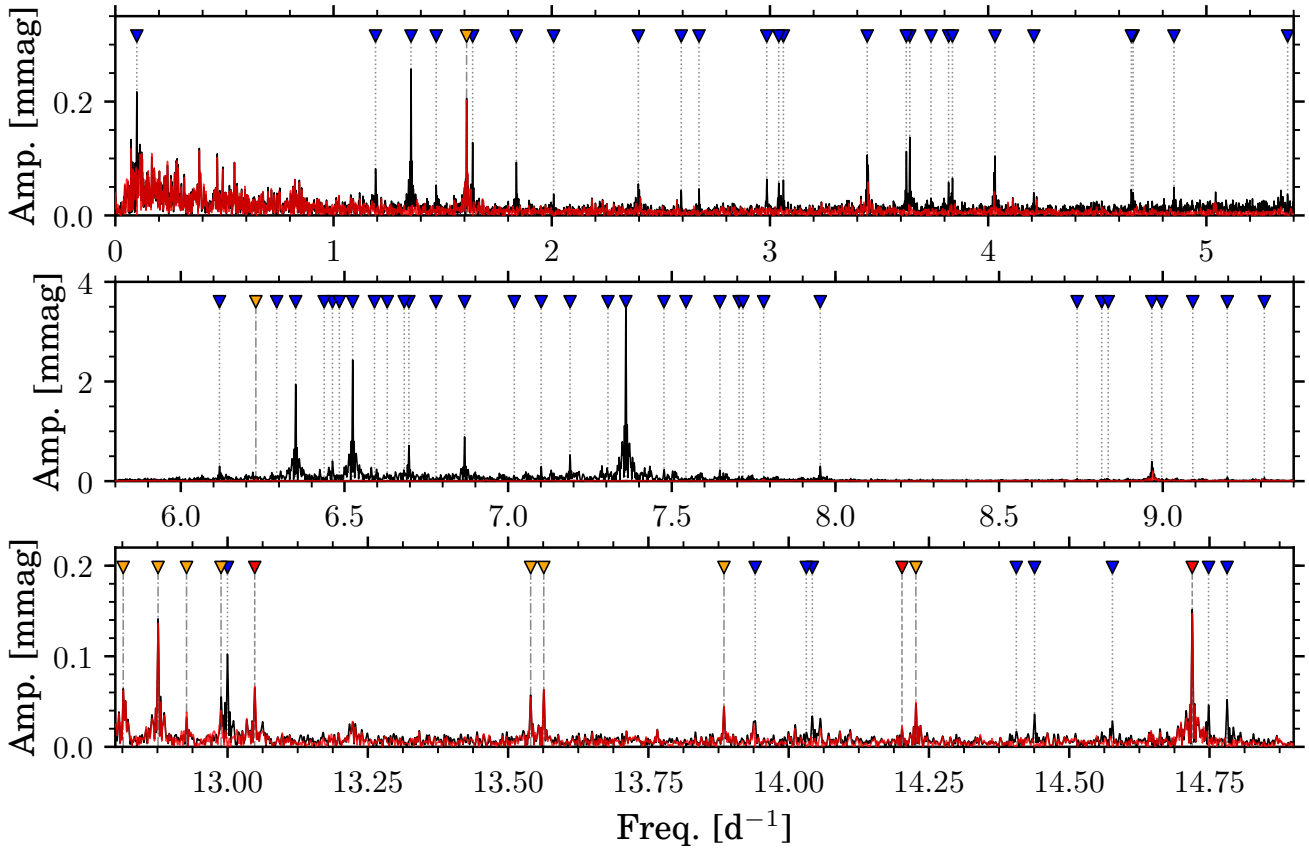

Fig. 4. Periodogram of our detrended SAP light curve from TESS of HD 192575 in three regimes of interest (black). The frequencies resulting from our iterative pre-whitening, filtering and non-linear least-square fitting analysis are marked with dotted grey lines and blue triangles. Combination frequencies are shown by orange triangles and dashdotted lines, and harmonic frequencies are shown by red triangles and dashed lines. The residuals after the final multi-frequency non-linear least-squares fit to the light curve are shown in red.

($0 \leq \ell \leq 3$) modes (Stankov & Handler 2005; Handler et al. 2006; Bowman 2020; Aerts 2021). In the case of a spherically symmetric star, frequencies of the same ℓ and $n_{\rm pg}$ but different m are degenerate. Deviations from spherical symmetry, notably rotation, effectively lift this degeneracy perturbing the frequencies of modes with different m values (Unno et al. 1989; Aerts et al. 2010). In a first-order perturbative approach, which is valid for slow rotation, the frequencies are given as follows:

$$f_{nlm} = f_{nl0} + m\beta_{nl} \int_0^R K_{nl}\Omega(r)dr, \quad (1)$$

where K_{nl} is the rotational kernel, $\Omega(r)$ the rotation profile of the star and $\beta_{nl} = (1 - C_{nl})$ with C_{nl} being the Ledoux constant (Ledoux 1951). Both β_{nl} and K_{nl} depend strongly on the mode properties and the interior structure of the star (Ledoux 1951; Aerts et al. 2011). Modes with $m = 0$ are historically referred to as zonal modes, modes with $m = |l|$ as sectoral and other modes as tesseral. In the case of rigid (solid-body) slow rotation, and assuming the pulsation axis coincides with the rotation axis, the frequency of mode $f_{n\ell m}$ can be given as:

$$f_{nlm} = f_{nl0} + \left(m\beta_{nl} f_{\rm rot}\right), \quad (2)$$

with $f_{\rm rot}$ the rotation frequency of the star (Aerts et al. 2011, 2019). In the case of low radial order p modes, $\beta_{nl} \in [0.5 - 1]$, depending on the stellar model, such that the frequency separation of rotationally-split modes in the amplitude spectrum of a slowly-rotating star provides information on the rotational frequency of the star (Aerts et al. 2010; Kurtz et al. 2014; Aerts et al. 2019; Bowman 2020). Identifying rotational splittings in the amplitude spectra of pulsating stars is therefore a powerful way to derive the angular degree ℓ and azimuthal order m of pulsation frequencies and derive the internal rotation properties of a star once the Ledoux constant is known from a stellar model.

The periodogram of our detrended SAP light curve shows significant periodic variability over a relatively large frequency range. We plot parts of the periodogram in Fig. 4, covering three frequency regions of interest. A clear dominant frequency is measured at $f_1 = 7.359625(1)$ d^{-1}, and four equally spaced frequencies at $f_3 = 6.350919(2)$ $f_2 = 6.525005(2)$, $f_5 = 6.696791(5)$, and $f_4 = 6.867008(4)$ d^{-1} (middle panel of Fig. 4). Harmonics and combinations of the dominant frequencies are found in the high frequency regime (in red and orange respectively), in addition to several independent modes (lower panel of Fig. 4). We also note the presence of low frequencies $1 < f < 5$ d^{-1} (top panel of Fig. 4) which fall in the g mode frequency domain and one frequency below < 1 d^{-1}, $f_{15} = 0.09852(2)$ d^{-1}, which can be signature of the rotation of the star (e.g. due to surface inhomogeneities) as discussed below.

The spacing of the equally spaced frequencies (f_3, f_2, f_5, f_4) $\Delta f \approx 0.17$ d^{-1}, motivated us to look for other similar spacings in periodogram. We collected all instances in Table 4 and sorted them into identified multiplets. Most convincing are the two higher amplitude quadruplets (quad1 and quad2), which are

Table 4. Frequency spacings and multiplets of interest detected in HD 192575.

Multiplet	Pair $f_x - f_y$	f_x (d^{-1})	f_y (d^{-1})	Δf (d^{-1})
	$\Delta f \sim 0.17$ d^{-1}			
quad1	$f_2 - f_3$	6.525005(2)	6.350919(2)	0.174087(3)
	$f_5 - f_2$	6.696791(5)	6.525005(2)	0.171786(6)
	$f_4 - f_5$	6.867008(4)	6.696791(5)	0.170217(7)
quad2	$f_{13} - f_{14}$	6.29283(2)	6.11813(2)	0.17470(2)
	$f_8 - f_{13}$	6.46341(1)	6.29283(2)	0.17058(2)
	$f_{17} - f_8$	6.63072(2)	6.46341(1)	0.16731(2)
trip1	$f_1 - f_6$	7.359625(1)	7.189246(8)	0.170379(8)
	$f_6 - f_{56}$	7.189246(8)	7.01888(9)	0.17037(9)
trip2	$f_{18} - f_{16}$	7.64721(2)	7.47607(2)	0.17114(3)
	$f_{16} - f_{70}$	7.47607(2)	7.3050(1)	0.1710(1)
trip3	$f_{62} - f_{76}$	14.74834(9)	14.5770(1)	0.1713(2)
	$f_{76} - f_{77}$	14.5770(1)	14.4057(2)	0.1713(3)
doub1	$f_{10} - f_{30}$	7.95372(1)	7.78074(5)	0.17298(5)
doub2	$f_{22} - f_{45}$	1.63748(4)	1.47036(8)	0.16712(8)
doub3	$f_{60} - f_{28}$	2.00851(9)	1.83767(4)	0.1708(1)
doub4	$f_{78} - f_{51}$	14.9525(2)	14.78131(7)	0.1712(2)
doub5	$f_{57} - f_{71}$	7.71751(9)	7.5433(1)	0.1742(2)
	$\Delta f > 0.17$ d^{-1}			
quint1	$f_{19} - f_{26}$	3.64072(3)	3.44556(4)	0.19516(5)
	$f_{35} - f_{19}$	3.83624(6)	3.64072(3)	0.19552(7)
	$f_{24} - f_{35}$	4.03104(4)	3.83624(6)	0.19480(8)
	$f_{48} - f_{24}$	4.20959(8)	4.03104(4)	0.17855(9)
quint2	$f_{37} - f_{65}$	9.31029(7)	9.0918(1)	0.2185(1)
	$f_{29} - f_{37}$	9.54270(5)	9.31029(7)	0.23241(9)
	$f_{40} - f_{29}$	9.78958(7)	9.54270(5)	0.24688(9)
	$f_{31} - f_{40}$	10.03443(6)	9.78958(7)	0.24485(9)

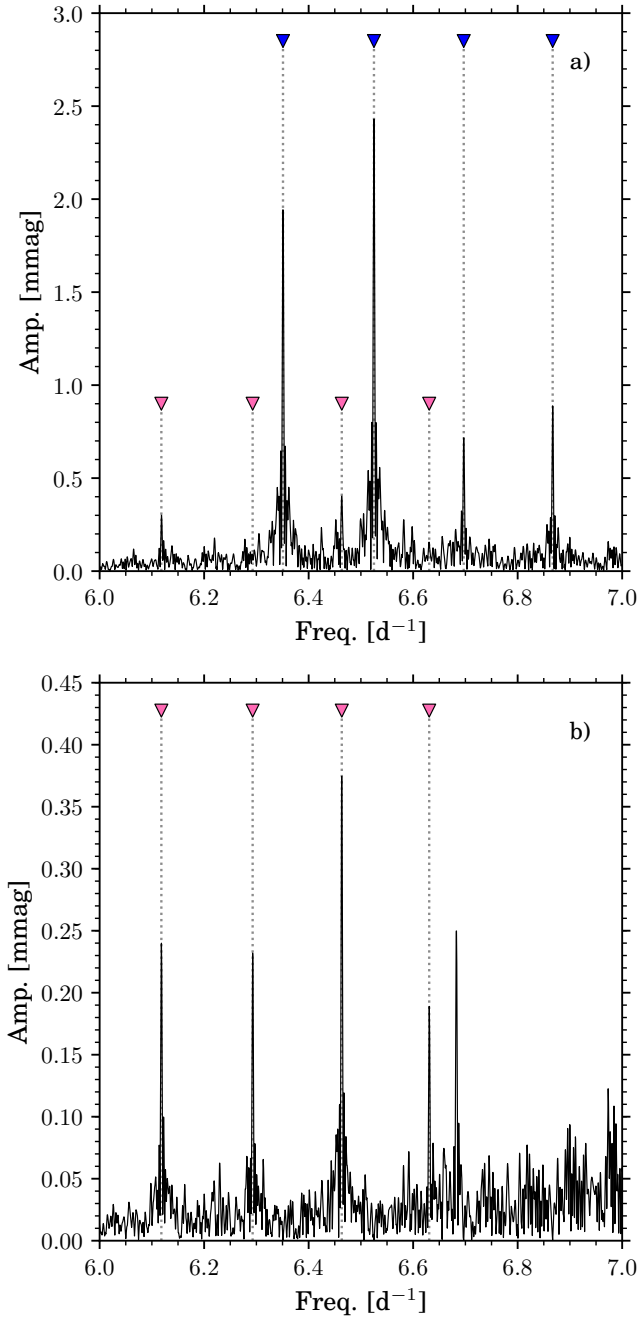

Fig. 5. Periodograms of the detected quadruplets with spacing $\Delta f \sim 0.17$ d^{-1} (quad1 and quad2 in the text). Panel a) shows the periodogram of the original signal with the high amplitude multiplet indicated by blue markers (f_3, f_2, f_5, f_4) and the lower amplitude multiplet by pink markers ($f_{14}, f_{13}, f_8, f_{17}$). In Panel b) we show the periodogram after extracting the high amplitude multiplet in Panel a), which reveals the lower amplitude multiplet more clearly.

indicative of rotational splittings of an $\ell \geq 2$ mode with one or more missing members. We plot these two quadruplets in Fig. 5, showing the notable amplitude difference between the two.

We find one low frequency, $f_{15} = 0.09852(2)$ d^{-1}, which can be a signature of rotation (Lee 2021). If we use the measured 0.17 d^{-1} spacing value and the rigid rotation approximation, Eq. (2), and assume a typical β_{nl} value range (pulsation models predict β_{nl} values between 0.85 – 0.95 for $\ell = 2$ p modes) we derive a rotation frequency $f_{\rm rot} \sim 0.18 - 0.20$ d^{-1}. The lowest measured frequency $f_{15} = 0.09852(2)$ d^{-1} is therefore consistent with the surface rotation frequency or a subharmonic thereof. That the 0.17 d^{-1} splitting is due to rotation also allows us to interpret the triplet containing the dominant frequency $f_1 = 7.359625(1)$ d^{-1} as an $\ell = 1$ triplet, see Fig. 6 and Table 4.

We also detect a low frequency quintuplet between $f \sim 3.5 - 4.0$ d^{-1}, with a higher average frequency splitting ($\Delta f \sim 0.178 - 0.195$ d^{-1}), as shown in Fig. 7 and Table 4. This multiplet is additionally bifurcated. Two of these splittings are resolved, the doublet in the centre (f_{33}, f_{35}) and the doublet centre-

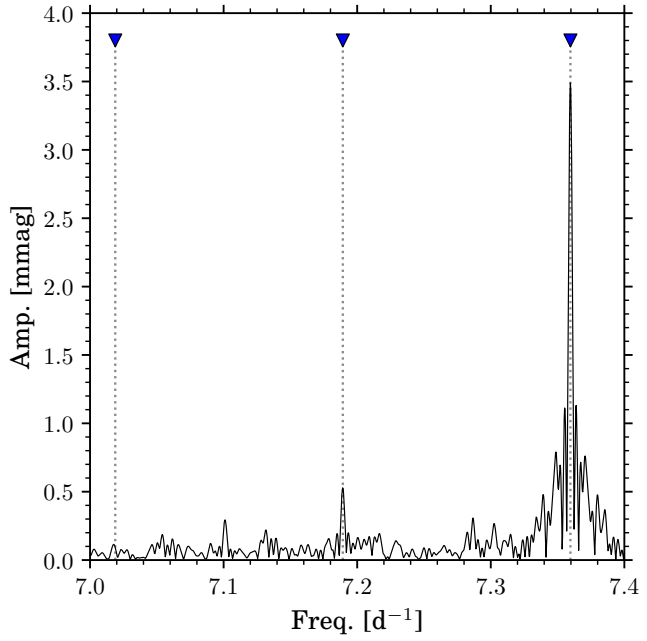

Fig. 6. Periodograms of the detected triplet around the dominant frequency (trip1 in the text). Note the large amplitude differences.

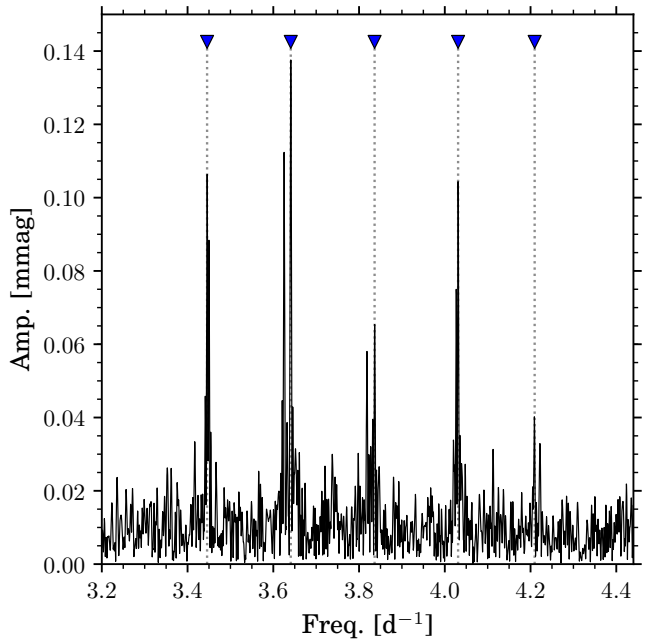

Fig. 7. Periodogram of the detected quintuplet with spacing $\Delta f \sim 0.17 - 0.19$ d^{-1} (quint1 in the text). Note that all members are bifurcated. For reasons of clarity we only highlighted the highest amplitude frequency of the respective pairs ($f_{26}, f_{19}, f_{35}, f_{24}, f_{48}$) in order of increasing frequency.

left (f_{19}, f_{25}). The small frequency splittings are of the order $\sim 0.01 - 0.02$ d^{-1}. If the multiplet is composed of $\ell \geq 2$ modes, it follows from Eq. (2) that the multiplet, relative to the other multiplets, either has a higher β_{nl} value, or that the probed mode cavity rotates faster, or both. We test these two hypotheses: faster rotation and/or different $\beta_{\rm nl}$ values in Section 5. Another quintuplet ($f_{65}, f_{37}, f_{29}, f_{40}, f_{31}$), again with higher splitting

Table 5. Grid boundaries and stepsizes.

Parameter	Low	High	Stepsize
$M_{\rm ini}$ [M$_\odot$]	9.0	21.5	0.5
$f_{\rm CBM}$	0.005	0.035	0.005
$X_{\rm c}$	0.250	0.701	0.01
	0.013	0.250	0.005
		Total:	17108

($\sim 0.23-0.24$ d^{-1}) is detected around $\sim 9.3-9.8$ d^{-1}, but at much lower amplitude.

4. Modelling procedure

Forward asteroseismic modelling of pulsation mode frequencies consists of quantitatively comparing observed mode frequencies $f_{nlm}^{\rm obs,i} \pm \sigma_{nlm}^{\rm obs,i}$ to theoretically predicted mode frequencies from stellar models $f_{nlm}^{\rm theo,i}$ for $i = 1, ..., N_f$, with N_f being the number of measured frequencies (Aerts 2021). The fitting procedure is non-trivial as theoretical uncertainties and correlations are difficult to quantify and typically dominate over the accumulated measurement uncertainties (Moya et al. 2008; Bowman & Michielsen 2021).

Aerts et al. (2018) formulated a methodological framework for modelling the pulsation mode frequencies of stars with a convective core that includes estimations of the variance of the theoretical predictions by using the Mahalanobis distance as a merit function to be minimised:

$$\theta_0 = \underset{\boldsymbol{\theta}}{\rm argmin}\{(\boldsymbol{Y}^{\rm theo}(\boldsymbol{\theta}) - \boldsymbol{Y}^{\rm obs})^\top (V + \Lambda)^{-1} (\boldsymbol{Y}^{\rm theo}(\boldsymbol{\theta}) - \boldsymbol{Y}^{\rm obs})\}, \quad (3)$$

where $\boldsymbol{\theta} = (\theta^1, \theta^2, ..., \theta^n)$ are the n parameters to be estimated (e.g. mass and age), $\boldsymbol{Y}^{\rm theo}(\boldsymbol{\theta}), \boldsymbol{Y}^{\rm obs}$ the theoretical predictions and observed values respectively (e.g. frequencies or periods), $V = {\rm var}(\boldsymbol{Y}^{\rm theo})$ the variance-covariance matrix representing the correlation structure within the grid of theoretical predictions, and Λ are the measured frequency precisions. The form of Eq. (3) is similar to a traditional χ^2 merit function, with the addition of the covariance matrix V. The fitting method of Aerts et al. (2018), however, allows for statistically appropriate parameter estimation and uncertainty estimation of internal physics such as core-boundary and envelope mixing profiles, see Michielsen et al. (2021) for application to the Slowly Pulsating B star (SPB) KIC 7760680.

Using the multiplets of rotationally-split non-radial pulsation modes (cf. Section 3.3) and the Mahalanobis distance as an estimator, we perform forward asteroseismic modelling to constrain a minimal set of parameters $\boldsymbol{\theta} = (M_{\rm ini}, X_{\rm c}, f_{\rm CBM})$, which are the mass, core hydrogen content, and the core-boundary mixing parameter (cf. *Problem 1* in Aerts et al. 2018). With these parameters derived we also gauge whether we are sensitive to the envelope mixing $D_{\rm env}$ of HD 192575 by including it as a free parameter.

4.1. Numerical setup

We calculate stellar models using the stellar evolution code MESA (Paxton et al. 2011, 2013, 2015, 2018, 2019, v.12778). We fix the initial composition ($X_{\rm ini}$, $Z_{\rm ini}$, and $Y_{\rm ini} = 1 - X_{\rm ini} - Z_{\rm ini}$)

and base it on the cosmic standard B star values of Nieva & Przybilla (2012). This is justified by our spectroscopic results which show no significant enrichment or deficiency of metals. We use the OP opacity tables (Seaton 2005) and the metal mixture by Nieva & Przybilla (2012). For the convective zones the Henyey formalism is employed (Henyey et al. 1965), with $\alpha_{\rm MLT} = 2.0$. The convective boundaries are determined through the Ledoux criterion and we use the MESA convective premixing scheme[3]. We further implement diffuse exponential core-boundary mixing based on the Herwig (2000) formalism, and apply this to core ($f_{\rm CBM}$), shell and envelope convective zones, setting the f_0 parameter (which determines how far into the convective zone the mixing is applied) to $f_0 = 0.005$. For the boundary mixing around shell and envelope convective zones containing little mass we fix the value at $f_{\rm shell,env} = 2f_0$ in order to smooth out the convective boundaries. We implement structured envelope mixing assuming a profile based on the internal gravity waves described in Pedersen et al. (2018) which originates from the hydro-dynamical simulations by Rogers & McElwaine (2017). In this formalism the diffusion coefficient depends on the local density as $D_{\rm mix}(r) \sim D_{\rm env} \cdot \rho^{-1}$. The stitching point at the base of the envelope $D_{\rm env}$ can the be varied to different levels. The stellar atmosphere is interpolated from photospheric tables (see Paxton et al. 2011, Sec. 5.3). Above 10000 K the Castelli & Kurucz model atmospheres (Castelli & Kurucz 2003) are used. No rotation is applied to the MESA models following the slow rotation of the star. Mass loss is calculated using the Vink et al. (2001) formalism scaled by a factor of 0.3 to conform to recent observational and theoretical results (Puls et al. 2015; Björklund et al. 2021). Mass loss rates in the considered mass regime tend to be small, for example a 21.5 $M_\odot$ model with $f_{\rm CBM} = 0.02$ in our set-up has a TAMS/ZAMS mass ratio of ~ 0.990, while a 9 $M_\odot$ model with $f_{\rm CBM} = 0.02$ in our set-up has a TAMS/ZAMS mass ratio of ~ 0.996. Appendix C provides the link to the full MESA inlists.

We start by computing a coarse grid covering the core-hydrogen burning phase, from the zero-age main sequence (ZAMS) until hydrogen core exhaustion at the terminal-age main sequence (TAMS), for masses $M_{\rm ini}$ between 9 and 21.50 $M_\odot$ in steps of 0.5 $M_\odot$ and a core-boundary mixing parameter $f_{\rm CBM}$ between 0.005 and 0.035 in steps of 0.005. Mixing at the base of the envelope is in the first instance fixed at $\log D_{\rm env} = 3.00$ dex. We cover core hydrogen fraction intervals of $\Delta X_c = 0.01$ from $X_c = 0.701$ to $X_c = 0.25$, then $\Delta X_c = 0.005$ to $X_c = 0.013$. This brings us to a total of 94 stellar models per evolutionary track of a given mass. These choices are motivated by the need to ensure adequate coverage of the spectroscopic parameter space.

Each non-rotating MESA model is perturbed using the stellar oscillation code GYRE (Townsend & Teitler 2013; Townsend et al. 2018; Goldstein & Townsend 2020, v.6.0.1). Based on previous modelling results of β Cep stars, we consider angular degrees $\ell = 0 - 4$, and radial orders $-7 \leq n_{\rm pg} \leq -1$ for g modes, $1 \leq n_{\rm pg} \leq 6$ for p modes, and the f mode with $n_{\rm pg} = 0$. We solve for adiabatic oscillations, and assume zonal modes ($m = 0$). The outer boundary condition is set to `UNNO` which follows the Unno et al. (1989) formulation. The final coarse grid contains 182 evolution tracks, 17108 pulsation models and 923832 zonal pulsation frequencies. Appendix C provides a link to example GYRE inlist.

[3] http://mesa.sourceforge.net/docs/r12778/controls_defaults.html#Convective_premixing

4.2. Radial order fitting the multiplets

We are able to infer the angular degree ℓ and azimuthal order m for the multiplets from the observed frequency splittings in the TESS data (cf. Section. 3.3). The radial order $n_{\rm pg}$ however needs to be derived by comparison with pulsation models. We achieve this by radial order fitting the zonal modes of the multiplets one-by-one, using the 3σ spectroscopic error box ($T_{\rm eff}$, $\log g$) as a constraint. We fit the zonal frequency of a multiplet as a certain angular degree using the MD and recover the possible radial orders within the spectroscopic error box. Next we add the zonal frequency of another multiplet for these radial orders and determine if it can be reconciled, and so on (see also Appendix D). We start with the following multiplets (and their zonal modes) as they are high amplitude and relatively isolated: quad1, quad2, trip1, and quint1 (cf. Table 4). Following this analysis we test if additional frequencies/multiplets are consistent with the resulting model fits. We conclude that angular degrees $\ell = 0, 1, 2$ are able to explain most multiplets but need to invoke higher angular degrees for additional multiplets.

4.2.1. The dominant quadruplet as a quadrupole mode

We initially focus on the dominant multiplet quad1 (f_3, f_2, f_5, f_4). We observe four members which implies an angular degree of at least $\ell \geq 2$, and that at least one mode frequency is not excited to observable amplitude in the TESS observations. The zonal mode is likely one of the two middle frequencies (see Fig. 5). To test whether the assumption of the zonal frequency makes a difference for the radial order we assume angular degree $\ell = 2$ and separately fit for the radial order for the zonal mode as the right-middle frequency (f_5) and the zonal mode as the left-middle frequency.

We show the results of this exercise in Fig. 8 in which the best solutions for the different radial orders appear as ridges. We find that radial orders f, p_1, p_2 are possible within the 3σ spectroscopic error box. Increasing radial orders lead to more massive and evolved stellar models which are not consistent with the spectroscopic error box. This result is independent of the zonal mode choice, either the left-middle frequency (a) or right-middle frequency (b), with slightly more evolved models being chosen for the former. Due to the lack of preference for the zonal mode as either the right-middle or left-middle member we continue with the left-middle frequency (f_2) as the zonal mode as it has the highest amplitude.

4.2.2. Avoided crossings

We find in the observations a second multiplet very close to the dominant multiplet referred to as quad1. This multiplet, quad2, also has four members ($f_{14}, f_{13}, f_8, f_{17}$) and is shifted towards lower frequency (cf. Fig 5). If we assume that both multiplets are $\ell = 2$ we find that such close frequency shifts between subsequent radial orders can only occur at so-called avoided crossings, which are a result of 'mode bumping' (Unno et al. 1989; Aizenman et al. 1977). This non-linear effect is caused by interacting p and g modes due to physical changes in their respective propagation zones, such as a receding convective core. This property can be exploited to derive stringent constraints on the age of the star (e.g. Mazumdar et al. (2006) in the case of β CMa).

To test whether HD 192575 exhibits pulsation modes undergoing an avoided crossing we plot the frequency evolution of $\ell = 2$ modes as a function of age for a range of masses and core-boundary mixing values in Fig. 9. Since avoided crossings in this

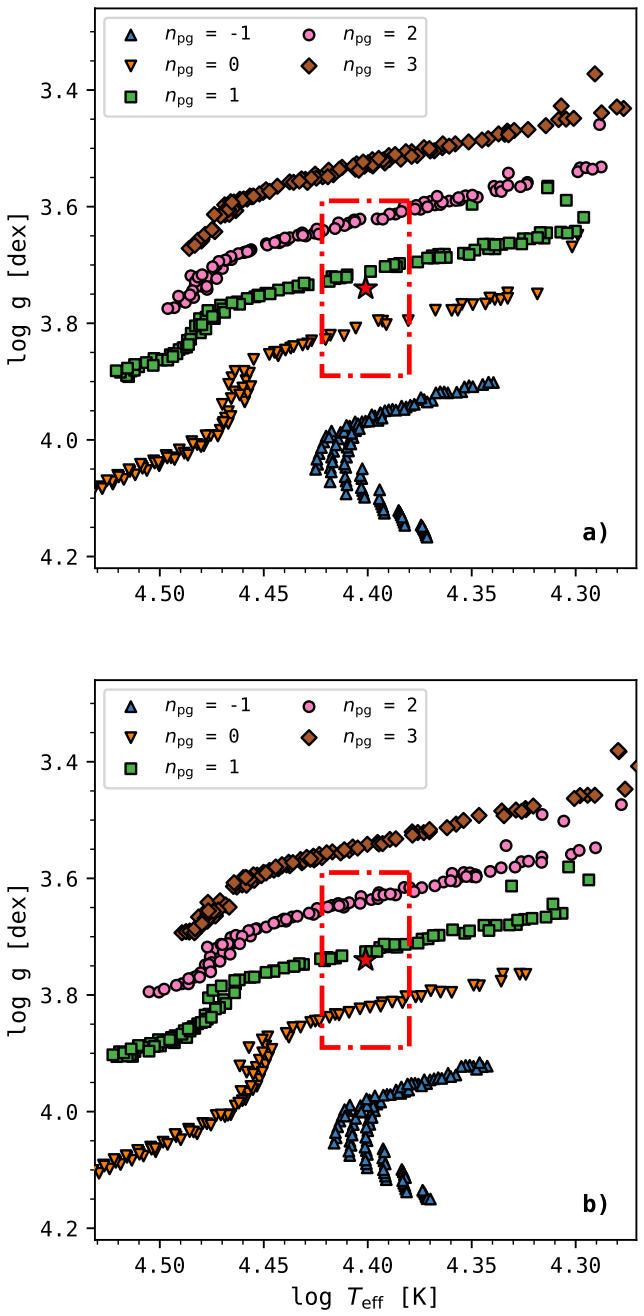

Fig. 8. Radial order fitting of quad1 as an $\ell = 2$ multiplet. Panel (a) shows the 100 best models of each fitted radial order as different symbols and colours in the case where f_2 is the zonal mode. Panel (b) in the case where f_5 is the zonal mode. HD 192575 and its 3σ spectroscopic error box are shown as a red star and a red dot-dash box respectively.

frequency regime mainly occur in the second half of the main sequence we plot models between $X_c = 0.40$ and $X_c = 0.01$. On Fig. 9 we find several avoided crossings, for example in the top left panel ($M_{ini} = 11.5\ M_\odot$, $f_{CBM} = 0.005$) an avoided crossing is seen at $X_c \sim 0.16$ (the g_1 and g_2 mode), after which the g_1 mode undergoes an avoided crossing with the f mode at $X_c \sim 0.09$, and so forth. The age at which modes experience avoided crossings is strongly dependent on the stellar model. In the considered frequency regime (horizontal dashed lines in Fig. 9 representing the two inner-left frequencies of the multiplets), we find that an $\ell = 2$ avoided crossing can only occur below $X_c \sim 0.05$ in all representative parameter combinations. However, none of these evolved models satisfy the 3σ spectroscopic error box. We therefore consider it unlikely that multiplets quad1 and quad2 are both $\ell = 2$ and close to an avoided crossing. The discovery of (at least) one $\ell > 2$ mode with such structured rotational splittings is an interesting result on its own. To establish the mode configuration of the other multiplets (i.e. trip1 and quint1) we focus on multiplet quad1 in the following sections.

4.2.3. Fitting the other multiplets

The triplet trip1 consists of frequencies f_{56}, f_6, f_1 in order of increasing frequency, and is therefore concluded to be a rotationally-split $\ell = 1$ triplet. We consider the best models in the 3σ spectroscopic error box obtained using the different radial orders for f_2 (quad1) in the last section. We first determine the possible radial orders of f_6 in the case where f_2 is an f ($\ell = 2$) zonal mode. In Fig. 10 we show the theoretical frequencies of the best models together with the fitted frequency (f_2) under this set of assumptions. We find that trip1 can be explained as an $p_2(\ell = 1)$ in most models. When we repeat the same exercise with f_2 as an $p_1(\ell = 2)$ zonal mode we find a higher radial order $p_3(\ell = 1)$ for f_6. For f_2 as an $p_2(\ell = 2)$ zonal mode, trip1 is found to be a $p_4(\ell = 1)$ triplet. This proves that the dominant frequency f_1 is not a radial mode but rather a prograde dipole mode. Thus we obtain three mode identification solution pairs for quint1 and trip1 that satisfy the atmospheric parameters, which are henceforth referred to as mode configurations A, B and C:

A) quad1: $p_2(\ell = 2)$ and trip1: $p_4(\ell = 1)$,
B) quad1: $p_1(\ell = 2)$ and trip1: $p_3(\ell = 1)$,
C) quad1: f ($\ell = 2$) and trip1: $p_2(\ell = 1)$.

We fit f_2 and f_6 with these three configurations in order to find the radial order of multiplet quint1 ($f_{26}, f_{19}, f_{35}, f_{24}, f_{48}$). For mode configurations B and C only a $g_2(\ell = 2)$ mode can explain the observed frequency range of quint1 (see Appendix D). However, for mode configuration A the mode identification of quint1 is non-trivial. In this case the frequency range of quint1 is consistent with multiple mode geometries. In fact, depending on the exact model, $g_1(\ell = 2)$, $g_2(\ell = 2)$, and $g_1(\ell = 1)$ modes occur in the frequency range of quint1 as shown in Fig. 11 for a representative model ($M_{ini} = 13.5\ M_\odot$, $f_{CBM} = 0.015$). The density of modes is explained by the evolved stage of the models in this mode identification where avoided crossings are more common. We investigate whether this close approach of the zonal modes may explain the bifurcation observed for several members of quint1 as a result of overlapping zonal and non-zonal modes (cf. Fig. 7).

Next we consider all frequencies of quint1 ($f_{26}, f_{19}, f_{35}, f_{24}, f_{48}$), including the resolved bifurcated members (f_{25}, f_{33}) belonging to the left-middle and centre doublets respectively. If these small splittings are the result of close approach of several multiplets we require at least two $\ell = 2$ multiplets (with at least four members each). The overlap of one $\ell = 2$ (five members) and one $\ell = 1$ (three members) multiplet would not reproduce all bifurcations. Similarly, two overlapping $\ell = 1$ multiplets (3 members each) are also unlikely since subsequent radial orders are too far apart in this frequency regime (see p_1, g_1, and g_2 ($\ell = 1$) as the triangles in Fig. 11) and not all bifurcations would be reproduced.

Since we require at least two $\ell = 2$ modes we test the hypothesis that the multiplet is just two overlapping $\ell = 2$ modes, which we refer to as quint1a and quint1b for the $g_2(\ell = 2)$ and $g_1(\ell = 2)$

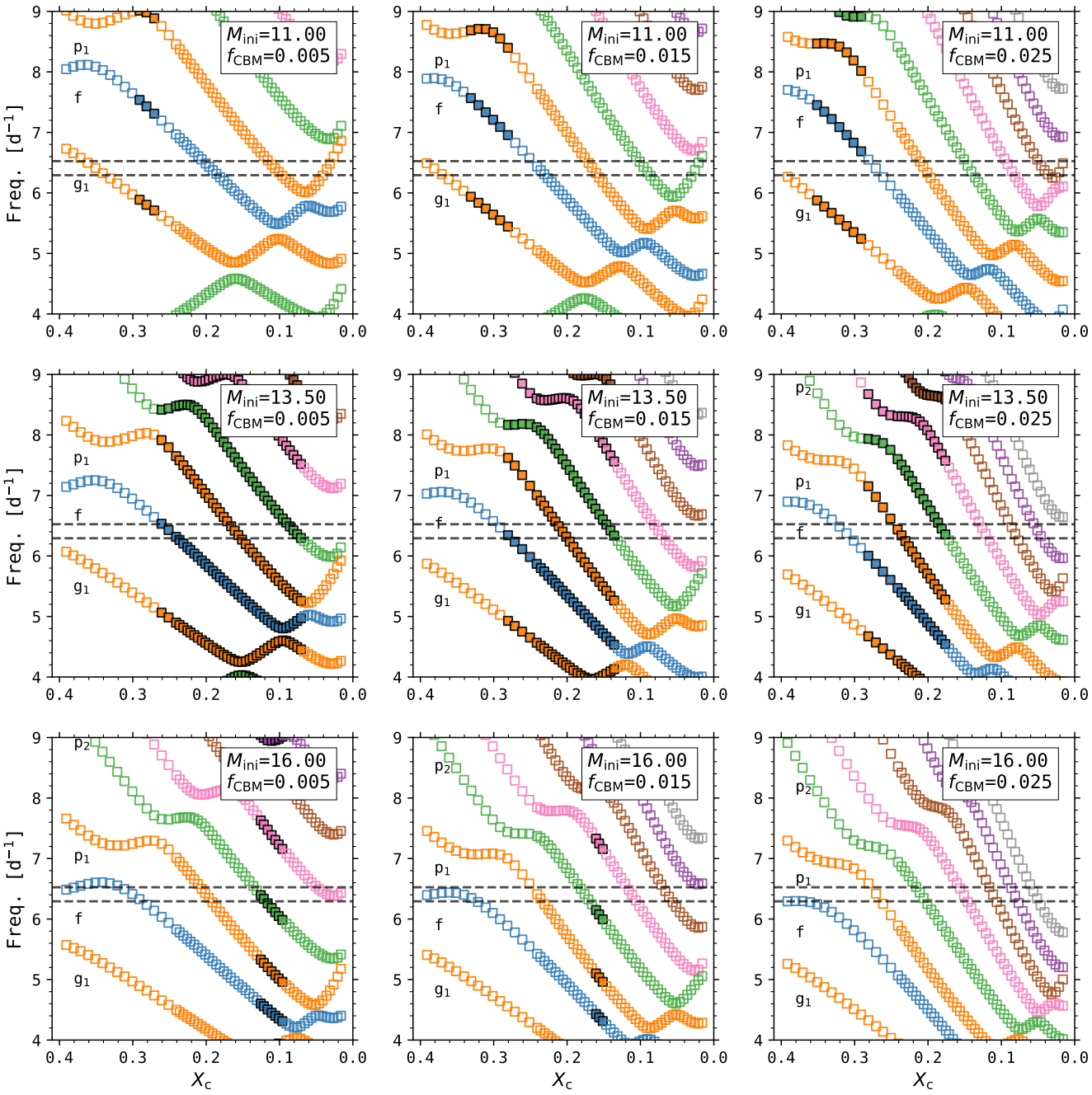

Fig. 9. Evolution of $\ell = 2$ modes as a function of core hydrogen content for different stellar models. Each panel shows the mode evolution for a stellar track between $X_c = 0.40$ and $X_c = 0.01$. Modes of different radial orders are given by squares of a different colour with the radial order given on the left. Filled and empty squares indicate models in and out of the 3σ spectroscopic error box, respectively. We plot frequencies f_2 and f_{13} as horizontal dashed lines.

mode, respectively. As shown in Fig. 11, we find that the closest approach of the $g_2(\ell = 2)$ and $g_1(\ell = 1)$ modes in this mass and age regime is about $\Delta f \sim 0.20$ d^{-1} which implies the frequency spacing between the zonal modes of quint1a and quint1b must be at least this value (approximately the large splitting distance between frequencies of quint1). Therefore we conclude that the zonal modes of quint1a/b cannot both be central in quint1, and that at least one of the close multiplets has a missing member .

This leaves three explanations. One option is that the zonal modes are the left-middle and middle frequencies of quint1 (f_{19}, f_{35}, where quint1a is a quadruplet and quint1b a quintuplet), the second option is that that the zonal modes are the middle and right-middle frequencies of quint1 (f_{35}, f_{24}, where quint1a is a quintuplet and quint1b a quadruplet) and the third option where the zonal modes are the right-middle and the left-middle frequencies (f_{19}, f_{24}, where quint1a/b are both quadruplets). We show these options schematically in Fig. 12. In the above scenarios we ignore the small frequency splitting between the bifurcated doublets since it is much smaller than the model precision. The first two options imply the star is at the closest approach of an avoided crossing between the $\ell = 2$ modes, severely limiting the number of valid models, and explains four out of five bifur-

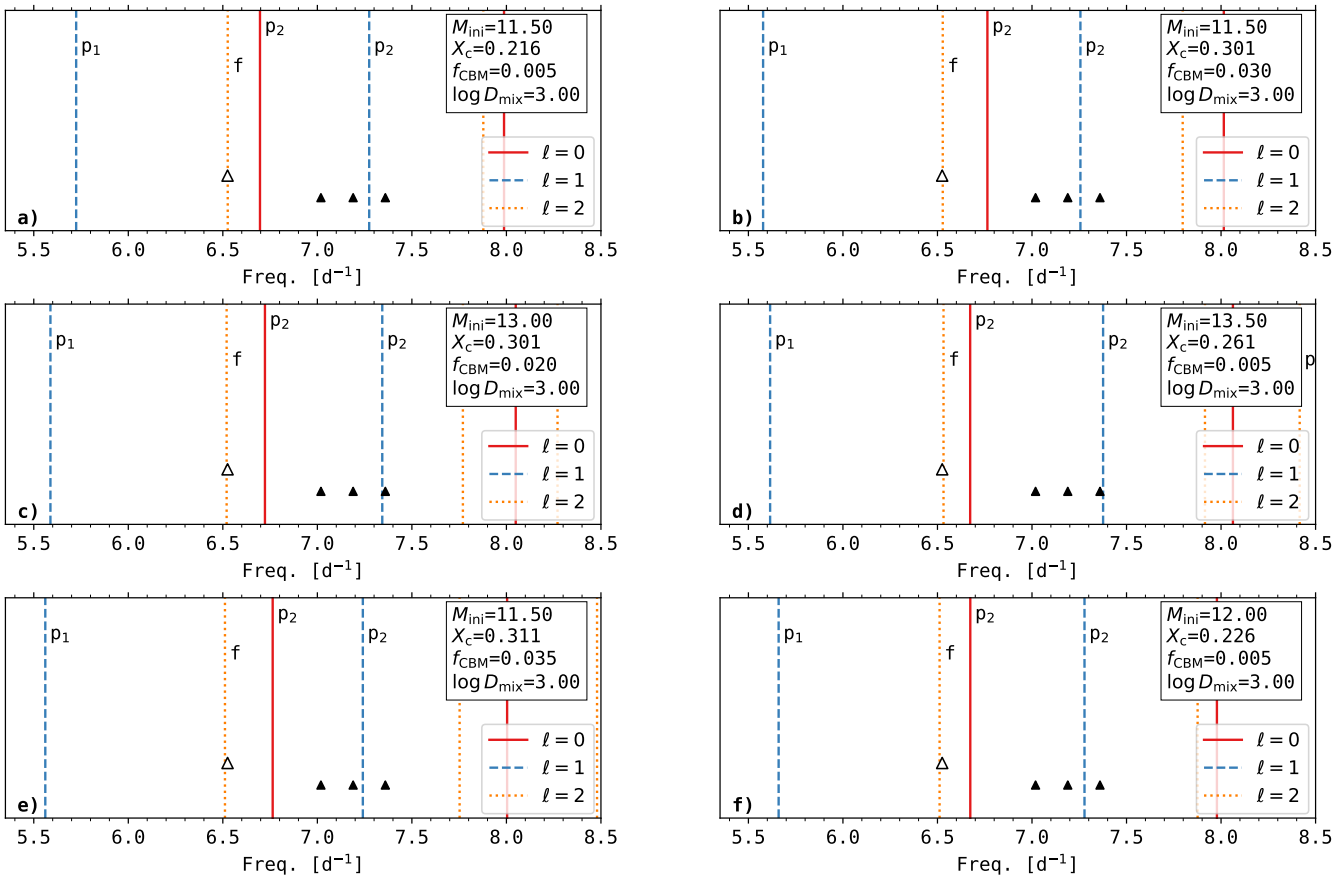

Fig. 10. Best models assuming f_2 is an $(\ell, n_{pg}) = (2, 0)$ zonal mode in the 3σ spectroscopic error box. The models are ranked according to their ascending MD value, from a) to f), with their parameters given on the top right. Red solid lines indicate radial modes $\ell = 0$, blue dashed lines are dipole modes $\ell = 1$ and orange dotted lines are quadrupole modes $\ell = 2$. The radial order can be found right of the frequency (e.g. f indicating an $n_{pg} = 0$ mode, and p_1 a mode of radial order $n_{pg} = 1$). The fitted frequency (f_2) is given by an empty triangle while the dark triangles indicated the non-fitted triplet frequencies (f_{56}, f_6, f_1).

cations. The missing bifurcation in these cases can be explained as a $g_1(\ell = 1)$ mode, given its close approach to $g_1(\ell = 2)$ and $g_1(\ell = 2)$ in Fig. 11. The third option allows the star to be either before or after the closest approach of an avoided crossing (cf. Fig. 11), increasing the number of valid models, and would explain the three central bifurcations. Here, the $g_1(\ell = 1)$ mode can also be invoked but it would explain only one additional bifurcation.

We test these three options by fitting the zonal frequencies, and find only the first and third option to reproduce the other multiplets in mode configuration A. This means that mode configuration A allows us to explain the bifurcated quintuplet as an avoided crossing between a $g_2(\ell = 2)$ (quint1a) and $g_1(\ell = 2)$ (quint1b) mode, which significantly narrows the possible models. Since it is difficult to decide between option 1 and 3, we opt for option 3 in order to avoid an underestimation of the X_c range. Nevertheless, these findings strongly favour mode configuration A since in the two other configurations (B & C) none of the stellar models are near an $\ell = 2$ avoided crossing in the quint1 frequency regime. This implies that higher ℓ modes (e.g. overlap between an $\ell = 2$ and $\ell = 4$ mode) or another mechanism must be invoked for these configurations in order to reproduce the observed bifurcations. We therefore drop mode configurations B and C from consideration.

Next we identify other observed multiplets and their corresponding frequencies (cf. Table 4) that are consistent with the fitted multiplets in mode configuration A. We found in Section 4.2.2 that the lower amplitude multiplet quad2 cannot be explained as $\ell = 2$. By looking at the best models in mode configuration A we find that only an $p_1(\ell = 4)$ mode can reproduce the frequency range of quad2, and therefore the close proximity of the two quadruplets. Moreover, the best models indicate that the $\ell = 2$ and $\ell = 4$ zonal mode frequencies should be very close which conforms to the observations. For other multiplets the mode identification is less straightforward. The radial order (and degree) of triplet trip2 are less certain as only $\ell > 2$ modes can explain its proximity to trip1. The highest frequency multiplet trip3 can only be explained by high order ($n_{pg} > 5$) and high degree ($\ell > 2$) modes. This is true for any frequency above ~ 12 d^{-1}. The other quintuplet, quint2, is likely $\ell = 2$ but its frequency range falls just in between radial orders $n_{pg} = 4$ and 5. We also search for single frequencies that can be explained as radial modes, e.g. the high amplitude single frequencies $f_8 = 8.96669(1)$ d^{-1} and $f_{20} = 9.19716(4)$ d^{-1} (cf. Fig. 4). However only one of these can be radial (at most), since the period ratio of the subsequent radial orders does not allow both to be radial for any parameter combination within the 3σ spectroscopic error box. In the lower frequency regime we measured several frequencies between $f \sim 1 - 3$ d^{-1}. The models predict a dense number of modes of degrees $\ell = 1$ ($n_{pg} \in [-3, -5]$) and $\ell = 2$ ($n_{pg} \in [-5, -7]$), which makes it difficult to disentangle their individual contributions. As a result, we conclude that we

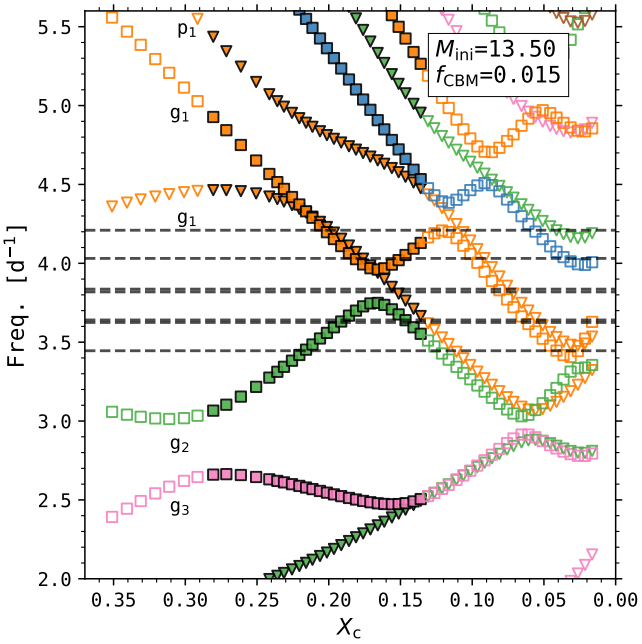

Fig. 11. Mode evolution of $\ell = 1, 2$ modes of a representative model in the frequency regime of quint1. Same layout as Fig. 9. Squares indicate $\ell = 2$ modes and triangles $\ell = 1$ modes. Colours indicate different radial orders, red for $|n_{\rm pg}| = 4$, pink for $|n_{\rm pg}| = 3$, green for $|n_{\rm pg}| = 2$, orange for $|n_{\rm pg}| = 1$, and blue for $n_{\rm pg} = 0$. The horizontal lines indicate the measured frequencies in quint1 $f_{26}, f_{19}, f_{25}, f_{33}, f_{35}, f_{24}, f_{48}$ in order of increasing frequency.

have reached the limit of a robust identification of radial orders given the data, and proceed with the current fitted multiplets and their mode configurations.

4.3. Best model determination

Armed with mode configuration A we now determine the final best model and the projected confidence inntervals for each model parameter. We first calculate the MD values over the whole model grid in order to capture the full correlation structure. We use frequencies $f_2(\ell = 2, n_{\rm pg} = 2)$, $f_6(\ell = 1, n_{\rm pg} = 4)$, $f_{19}(\ell = 2, n_{\rm pg} = -2)$ and $f_{24}(\ell = 2, n_{\rm pg} = -1)$ as the fitted zonal frequencies. We do not fit quad2 as there are five missing members making it difficult to assign the zonal mode despite most models predicting it close to f_2. We then proceed by cutting models according to two criteria. Firstly the models need to satisfy the 3σ spectroscopic constraints. Secondly the bifurcations must be explained by an avoided crossing. For the latter this means that we filter out models where the difference between the theoretical $g_2(\ell = 2)$ (quint1a) and $g_1(\ell = 2)$ (quint1b) modes is higher than the difference between observed frequencies f_{19} and f_{24}, using a 15% uncertainty range.

We then proceed with an error determination on the remaining models for which we use the likelihood function associated with the Mahalanobis distance (Eq. 3) in combination with Bayes' theorem (e.g. Mombarg et al. 2021; Michielsen et al. 2021). That is, we find the likelihood of parameters $\boldsymbol{\theta} = (\theta^1, \theta^2, ..., \theta^k)$ given the observed data $\boldsymbol{D}$:

$$\mathcal{L}(\boldsymbol{\theta}|\boldsymbol{D}) = \exp\Big(-\frac{1}{2}(\ln(|V + \Lambda|) + k\ln(2\pi) + \mathrm{MD})\Big), \quad (4)$$

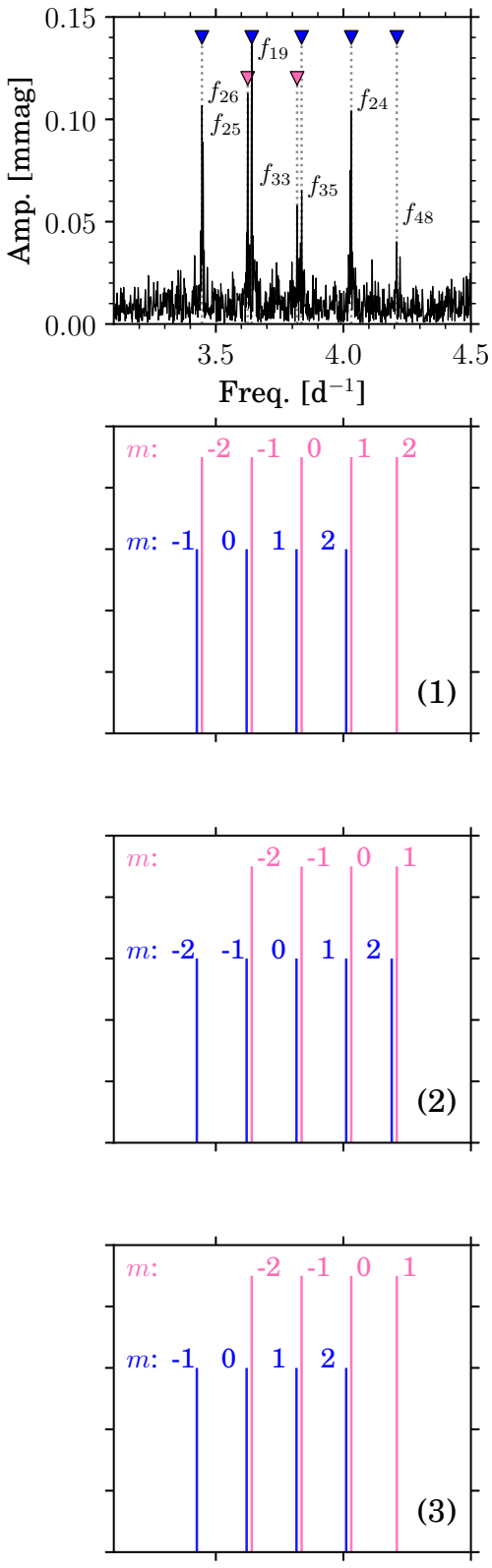

Fig. 12. Reproducing the observed bifurcations of quint1 in mode configuration A. The top panel shows the observed quintuplet with frequencies marked by blue and pink markers for the highest amplitude ($f_{26}, f_{19}, f_{35}, f_{24}, f_{48}$) and bifurcated members (f_{25}, f_{33}) respectively. The lower three panels show the possible overlap options considered in the text. The g_1 and g_2 mode are given in pink and blue, respectively, with the m values given to the right/left of each frequency. The relative amplitudes and small frequency shifts are fixed artificially in order to highlight the options more clearly.

Table 6. Best model and its 1σ confidence intervals using Bayes' theorem for HD 192575. The second column shows the result for varied $M_{\rm ini}, X_{\rm c}, f_{\rm CBM}$ and a fixed $D_{\rm env}$. The third column shows a comparison where $D_{\rm env}$ was varied as well. The inferred parameters are the age, the convective core mass $M_{\rm cc}$ and the stellar radius $R_{\rm cc}$.

Parameter	Value ($D_{\rm env}$ fixed)	Value ($D_{\rm env}$ varied)
$M_{\rm ini}$ [$M_\odot$]	$13.0^{+3.5}_{-0.5}$	$13.0^{+3.5}_{-0.5}$
$X_{\rm c}$	$0.156^{+0.050}_{-0.055}$	$0.156^{+0.055}_{-0.055}$
$f_{\rm CBM}$	$0.020^{+0.015}_{-0.015}$	$0.020^{+0.015}_{-0.015}$
$\log D_{\rm env}$ [dex]	3.0	$2.0^{+3.0}_{-0.0}$
Age [Myr]	$14.1^{+1.7}_{-4.6}$	$14.1^{+1.9}_{-4.6}$
$M_{\rm cc}$ [$M_\odot$]	$3.0^{+1.3}_{-0.3}$	$3.0^{+1.3}_{-0.4}$
$R_\star$ [$R_\odot$]	$9.5^{+1.2}_{-0.8}$	$9.5^{+1.2}_{-0.8}$

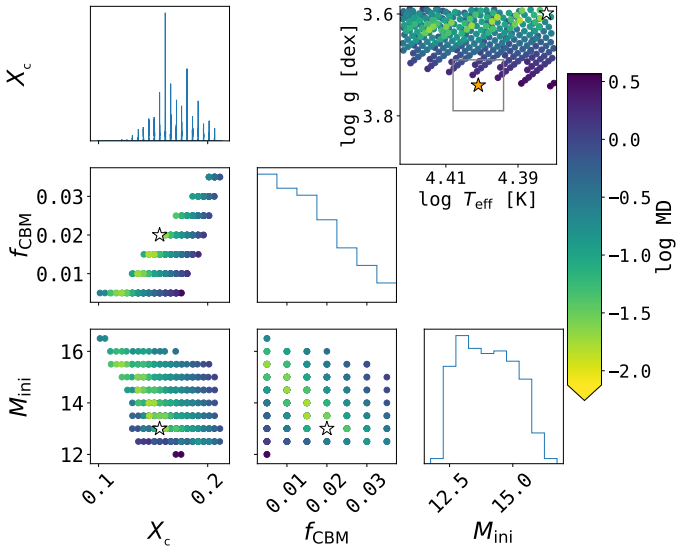

Fig. 13. Parameter correlation plot of the best models using the MD as an estimator. The best fitting model is shown as a white star. Only models in the 3σ spectroscopic error box and that satisfy the small frequency splitting of the bifurcation. The top right panel shows the Kiel diagram of all models in the 3σ spectroscopic error box. The orange star and grey box indicate the spectroscopic parameters and the 1σ spectroscopic error box of the star, respectively. The axis limits are set to the 3σ spectroscopic error box range.

where k is the number of free parameters, and MD the Mahalanobis distance, Eq. (3), of a certain set of parameters $\boldsymbol{\theta}$ (Aerts et al. 2018; Mombarg et al. 2021; Michielsen et al. 2021). As this is proportional to the probability density function $\mathcal{L}(\boldsymbol{\theta}|\boldsymbol{D}) \sim P(\boldsymbol{D}|\boldsymbol{\theta})$ we can apply Bayes' theorem which allows us to describe the probability of a parameter θ^m occurring in range $\theta^m \in [\theta^m_a, \theta^m_b]$ as:

$$P(\theta^m_a < \theta^m < \theta^m_b|\boldsymbol{D}) = \frac{\Sigma^q_i P(\boldsymbol{D}|\boldsymbol{\theta}_i)P(\boldsymbol{\theta}_i)}{\Sigma^Q_j P(\boldsymbol{D}|\boldsymbol{\theta}_j)P(\boldsymbol{\theta}_j)}, \tag{5}$$

where the denominator is a summation over the remaining models $j = 1, \ldots, Q$, and the nominator is a summation over all models $i = 1, \ldots, q$ with the highest likelihood such that $P(\theta^m_a < \theta^m < \theta^m_b|\boldsymbol{D}) = 0.68$. In our case $\boldsymbol{\theta} = (M_{\rm ini}, X_{\rm c}, f_{\rm ov})$ and $k = 3$.

We show the results of our parameter uncertainty calculation in Table 6. We find good constraints on the mass $M_{\rm ini}$ and central hydrogen content $X_{\rm c}$. Such a result is a clear demonstration of the probing power of constraining the properties of single stars down to comparable level that is achieved for eclipsing binary systems. The core-boundary mixing $f_{\rm CBM}$ propagates into the mass uncertainty interval, but nonetheless confirms the conclusion that stellar evolution codes underpredict the convective cores of main sequence stars (Pols et al. 1997; Higl & Weiss 2017; Claret & Torres 2019; Tkachenko et al. 2020; Pedersen et al. 2021). Our result is the first confirmation of this among single high mass stars using modern modelling techniques. The solution suggests a medium amount of convective boundary mixing, but the 1σ confidence interval spans the entire considered parameter range. We show the parameter correlations of the final models in Fig. 13, where the correlation between $M_{\rm ini}$ and $f_{\rm CBM}$ is clearly seen. Among the best models, lower mass models generally have higher core-boundary mixing values, and vice versa. Because of this correlation it is useful to consider the inferred core mass instead ($M_{\rm cc} = 3.0^{+1.3}_{-0.3}$ $M_\odot$[4]). We plot the histogram of the inferred core mass distribution within the confidence intervals of $M_{\rm ini}$, $f_{\rm CBM}$ and $X_{\rm c}$ on Fig. 14. This distribution is narrower than the distribution of $f_{\rm CBM}$ and more similar to the distribution of $M_{\rm ini}$ (cf. Fig. 13). The estimated core mass implies a core mass fraction $M_{\rm cc}/M_\star = 24 \pm 6$ % which conforms to estimates from binary studies in the same mass regime (Tkachenko et al. 2020).

We find in Fig. 13 that the error ellipsoid is well covered by the 3σ error box, except for the low temperature end. Furthermore, we note that the atmospheric parameters of the best asteroseismic model ($T_{\rm eff,seism} = 24100$ K, $\log g_{\rm seism} = 3.60$ dex) place it at the edge of the 3σ spectroscopic temperature $T_{\rm eff,spec} = 25200 \pm 400$ and surface gravity $\log g_{\rm spec} = 3.74 \pm 0.05$ estimates. A discrepancy between asteroseismic and spectroscopic $\log g$ of β Cep stars has been noted in the literature before, notably in the cases of θ Oph (Briquet et al. 2007), HD 46202 (Briquet et al. 2011), and HD 180642 (Aerts et al. 2011). In this temperature regime $\log g$ is often determined using the Balmer line wings which are very sensitive to both reduction techniques and the physics considered in the stellar atmosphere models. Temperature estimates on the other hand, are generally less affected by these issues as they rely on the Si ionisation balance. However since $\log g$ and $T_{\rm eff}$ are correlated we would need higher S/N spectra to investigate this in detail. For now, the spectra are sufficient to derive a good forward model of HD 192575.

4.4. Effect of envelope mixing

The shape and amount of envelope mixing necessary to explain observations of massive stars is a heavily researched topic in current stellar astrophysics. In particular the surface nitrogen abundance in main-sequence OB-type stars can be used to infer whether an efficient mixing mechanism is transporting this CNO cycle byproduct from the core to the surface (Hunter et al. 2008, 2009; Dufton et al. 2018). In rotating stars this enhanced abundance is explained by the combined effects of meriodional circulation, shear mixing and turbulence (e.g. Brott et al. 2011; Georgy et al. 2013). However, in some slowly rotating stars ($v \sin i < 50$ km s^{-1}) rotationally induced mixing alone is not enough to explain the enriched abundances (Hunter et al.

[4] This is the mass contained within the convective core as defined by the Ledoux criterion and does not include the core-boundary mixing region.

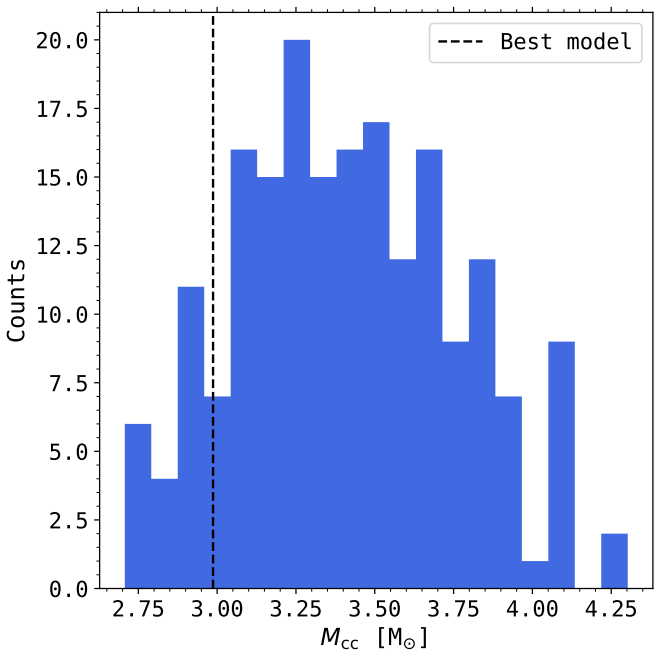

Fig. 14. Histogram of the inferred convective core masses M_{cc} within the confidence intervals of M_{ini}, f_{CBM} and X_c.

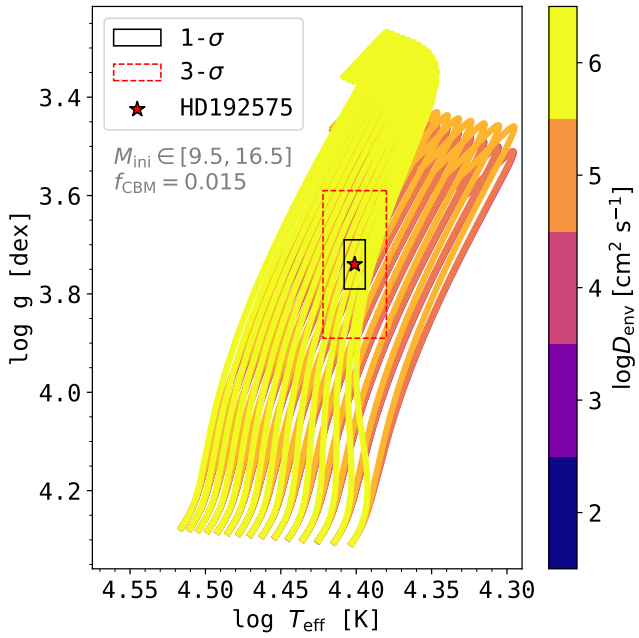

Fig. 15. Kiel diagram of the evolutionary tracks with increased envelope mixing $\log D_{env}$. Higher D_{env} values are stacked on top of lower D_{env} to highlight the changes. For demonstrative purposes the core-boundary mixing f_{CBM} was fixed at $f_{CBM} = 0.015$.

2008). A second proposed mechanism is pulsational mixing, which is supported by the observed correlations between pulsation frequencies and surface nitrogen enrichment (Aerts et al. 2014). Pulsational mixing includes internal gravity waves which have shown to induce efficient chemical mixing in the envelope (Rogers & McElwaine 2017).

This second mechanism is certainly promising for β Cep stars, since they are often slowly rotating, yet in some cases

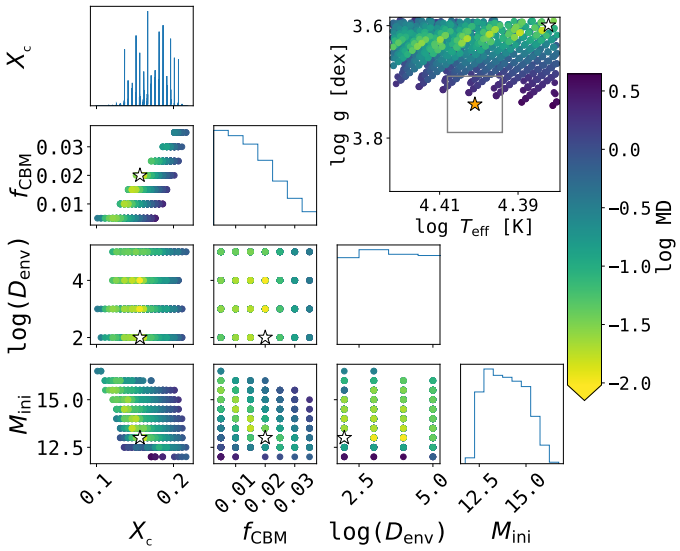

Fig. 16. Parameter correlation plot for the solution in the extended $\log D_{env}$ grid. Same layout as Fig. 13.

still show significant nitrogen enrichment at the surface (Morel et al. 2006). This makes them ideal candidates to test the envelope physics which includes the description and degree of envelope mixing. In the numerical setup we already applied the the internal gravity wave mixing wave formalism (Rogers & McElwaine 2017) since HD 192575 is a slow rotator ($v \sin i = 27^{+6}_{-8}$ km s^{-1}). We focus on a refined the mass extent of our grid ($M_{ini} \in [9.50, 15.00]$ in steps of 0.5 $M_\odot$), keep the sample range in f_{CBM}, and vary the envelope mixing at the base of the envelope ($\log D_{env} \in [2.00, 5.00]$ in steps of 1.00 dex), which was previously set to $\log D_{env} = 3.00$ dex. The reason we consider $\log D_{env} = 5.00$ dex as the cut-off is that significant blueward evolution of our MESA models starts to occur between $\log D_{env} = 5.00$ and 6.00 dex due to increased chemical homogeneity in the star, see Fig. 15. We find that for envelope mixing values between $\log D_{env} = 2.00$ and 4.00 dex differences in atmospheric parameters are barely noticeable. Only from $\log D_{env} = 4.00 - 5.00$ dex the evolutionary tracks start to shift slightly, with large changes for $\log D_{env} = 6.00$ dex as the stars starts to become increasingly near-fully mixed.

We determine a best model following our previous method (cf. Section 4.3). The free parameters are now $\boldsymbol{\theta} = (M_{ini}, X_c, f_{CBM}, \log D_{env})$. The addition of an extra parameter in the calculation of the correlation structure increases the lowest MD value, $\log \mathrm{MD} = 1 \cdot 10^{-2}$, relative to the value in the previous Section 4.3, $\log \mathrm{MD} = 7 \cdot 10^{-3}$. We show the results and calculation of confidence intervals in Table 6 and the parameter correlations in Fig. 16. We find the overall parameters consistent with the parameters derived using the $\log D_{env} = 3.00$ dex grid. The confidence intervals are found to be consistent as well except for a small increase for X_c and age (cf. Table 6). The best fitting model is now lower in envelope mixing, even though the confidence interval on the latter covers the full extent of considered grid. Moreover, we find that the second and third best fitting models have the same parameter combination with the exception of $\log D_{env} = 4.0$ and $\log D_{env} = 3.0$, respectively. We conclude that we are only slightly sensitive to the envelope mixing and favour the grid with fewer free parameters (and lower MD value) given the current available information. To improve the estimate of the envelope mixing in HD 192575 direct comparisons between the model and spectroscopic abundances are required. In

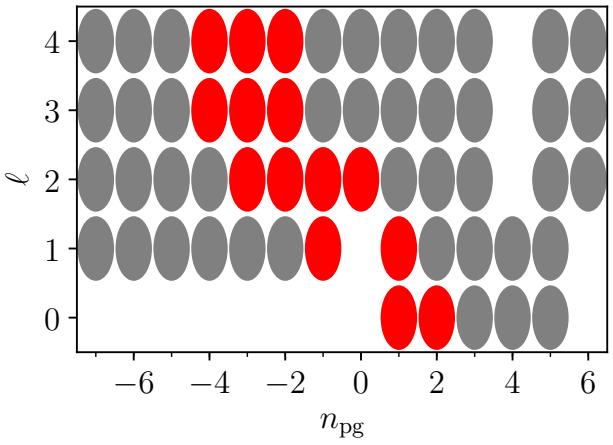

Fig. 17. Mode excitation in the best model obtained in Section 4.3. The angular degree ℓ is given on the vertical axis and the radial order $n_{\rm pg}$ on the horizontal axis. Red and grey markers indicate excited and damped modes, respectively.

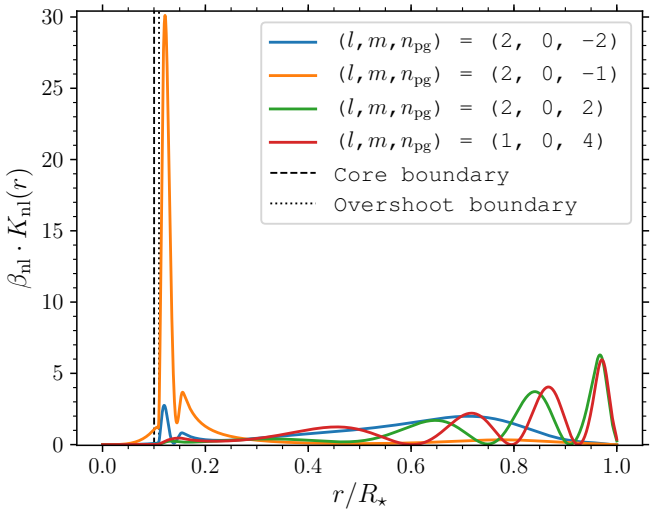

Fig. 18. Rotational kernel $\beta_{\rm nl} K_{\rm nl}$ as a function of the stellar radius. The vertical dashed and dotted lines show the boundary of the core and core-boundary mixing region respectively.

order to derive sufficiently small error margins on the latter we need very high S/N, higher than the S/N of the currently available spectra for HD 192575 (cf. Table 2).

4.5. Mode excitation of best model

We investigate the mode excitation in the best model (cf. Table 6) by calculating non-adiabatic pulsation models which provide linear growth and damping rates through the complex eigenfrequencies. We include non-adiabatic effects in GYRE v.6.0.1 using the standard method. This method first solves for the initial roots of the (complex) problem in the adiabatic approximation and then iteratively converges on the complex solution (Townsend et al. 2013, 2018; Goldstein & Townsend 2020)[5]. To determine excitation we use the sign of the imaginary frequency which is positive and negative for excited and damped modes, respectively.

We show the results of this exercise in Fig. 17. In some cases a non-adiabatic solution was not found, for example for modes of radial orders $n_{\rm pg} = 4$ and $n_{\rm pg} = 6$. This can happen if the mode growth rate is large or if the mode is strongly non-adiabatic. We find that for $\ell = 1$ radial orders between $n_{\rm pg} \in [-1, +1]$ are excited. For $\ell = 2$ this range is limited to $n_{\rm pg} \in [-3, 0]$. Therefore, not all observed modes are predicted to be excited in this model. This includes the high frequency (and thus higher radial order) multiplets quad1 ($\ell = 2, n_{\rm pg} = 2$), trip1 ($\ell = 1, n_{\rm pg} = 4$) and quad2 ($\ell = 4, n_{\rm pg} = 1$). We also note that while the quint1a and quint1b multiplets are excited, lower frequencies ($f < 3.4$ d^{-1}) are generally not predicted to be so. Therefore, far more excited pulsation modes are observed than predicted by models.

Similar excitation differences have been found in β Cep stars before, notably 12 Lac and ν Eri which also have both g and p modes (Dziembowski & Pamyatnykh 2008; Daszyńska-Daszkiewicz et al. 2017). Proposed solutions include the use of different opacity tables and local enhancements to the pulsation-driving region (Walczak et al. 2015; Daszyńska-Daszkiewicz et al. 2017). In the case of HD 192575 the latter could provide a solution since we already employ the OP opacity tables which have been shown to excite more modes than in the case of the OPAL tables (Miglio et al. 2007a,b), but this goes beyond the scope of this paper.

[5] See also https://gyre.readthedocs.io/en/stable/user-guide/non-ad-calculations.html

Table 7. Rotation frequencies derived from rigid rotation models for each of the multiplets.

Multiplet	$\beta_{\rm nl}$	$f_{\rm rot}$ (d^{-1})	$v_{\rm eq}$ (km s^{-1})
$p_4(\ell = 1)$	0.9687	0.176	84.25
$p_2(\ell = 2)$	0.8950	0.192	91.91
$g_1(\ell = 2)$	0.8791	0.219	104.8
$g_2(\ell = 2)$	0.8519	0.232	111.1

5. Precise constraints on non-rigid rotation profile

5.1. Rigid rotation model

Armed with the best model (cf. Table 6) we derive the rotation frequency directly from the frequency multiplets. We assume the theoretical frequency splittings are given by a rigid rotation model, Eq. (2), and derive $f_{\rm rot}$ using the $\beta_{\rm nl}$ from the model and $\Delta f = f_{nlm} - f_{nl0}$ from the data. For the overlapping multiplet, quint1, we use choose the left frequency in the two doublets for the g_2 modes and the right frequency for the g_1 modes (cf. Panel 3 in Fig. 12). This is an assumption but we find that the derived $f_{\rm rot}$ is unchanged within uncertainty if we assign different frequencies (see Appendix E).

We do this for all multiplets separately by means of a χ^2-minimisation (see Appendix E for details of the calculation). The results of this exercise are shown in Table 7. From this table we find that the observations are inconsistent with the rigid rotation assumption. Irrespective of the best model a higher rotation frequency is derived for the g mode multiplets than for the p mode multiplets. The maximum difference in derived rotation rate among the different multiplets is about 17%.

Table 8. Average splittings Δf and rotational kernel integrals for the calculation of the core and envelope rotation rates.

Multiplet	Δf (d^{-1})	K_0	K_1
$p_4(\ell = 1)$	0.17037(5)	0.0002	0.9685
$g_1(\ell = 2)$	0.18962(4)	0.0274	0.8517

5.2. Three-zone model

A more appropriate treatment of interior rotation is to use Eq. (1) which does not assume rigid rotation. The theoretical frequency splittings depend on the rotational kernel $\beta_{nl}K_{nl}(r)$ which is multiplied by the rotation profile $\Omega(r)$. We plot the $\beta_{nl}K_{nl}(r)$ profiles for the best model in Fig. 18. Clearly the $g_1(\ell = 2)$ and $g_1(\ell = 2)$ multiplets are much more sensitive to the near-core physics than the $p_4(\ell = 1)$ and $p_2(\ell = 2)$ multiplets which probe the outer envelope physics. We show the near-core region properties of the best model in Fig. 19. On Panel a) we find the mixing properties which show the μ gradient left behind by the receding core at this point in the stars' evolution. The resulting Brunt-Väisälä profile is shown in Panel b) of Fig. 19. The g modes are largely trapped in the μ-gradient zone left behind by the receding core. Such 'g_c' modes (as first termed by Dziembowski & Pamyatnykh 1991) have excellent probing power in the near-core regions and the rotational splittings therefore provide direct information about the local rotation rate.

As a result, the measurement of a higher rotation frequency from the identified g_c modes is evidence that the near-core region is rotating faster than the envelope, indicating radial differential rotation. To quantify the magnitude of the differential rotation we consider the following three-zone model of the rotation rate $\Omega(x)$ as a function of the fractional radius x (Pamyatnykh et al. 2004; Dziembowski & Pamyatnykh 2008):

$$\Omega(x) = \begin{cases} \Omega_{cc} & \text{if } x \leq x_{cc} \\ \Omega_{cc} + (\Omega_{cc} - \Omega_{env})\frac{x - x_{cc}}{x_{cc} - x_{CBM}} & \text{if } x_{cc} \leq x \leq x_{CBM} \\ \Omega_{env} & \text{if } x \geq x_{CBM}, \end{cases} \quad (6)$$

where $\Omega_{cc}, \Omega_{env}$ are uniform rotation rates in the core and envelope respectively, and x_{cc}, x_{CBM} the fractional radii of the core and the core-boundary mixing regions respectively. The physical representation of this model is a fast-rotating core and a slow envelope, divided by the core-boundary mixing region where a sharp decrease in the rotation rate occurs. We measure the unknown Ω_{cc}, and Ω_{env} from the measured frequency splittings by constructing a system of equations using Eq. (1) and Eq. (6). This yields the following system for measured frequency splittings $\Delta f_p, \Delta f_g$:

$$2\pi\Delta f_p = \Omega_{cc} \cdot K_{0,p} + \Omega_{env} K_{1,p} \quad (7)$$

$$2\pi\Delta f_g = \Omega_{cc} \cdot K_{0,g} + \Omega_{env} K_{1,g}, \quad (8)$$

where $K_{0,p/g}, K_{1,p/g}$ are integrals over the fractional radius,

$$K_{0,p/g} = \int_0^{x_{CBM}} \beta_{nl}K_{nl}(x)dx + \int_{x_{cc}}^{x_{CBM}} \frac{x - x_{cc}}{x_{cc} - x_{CBM}} \beta_{nl}K_{nl}(x)dx \quad (9)$$

$$K_{1,p/g} = \int_{x_{CBM}}^{R_\star} \beta_{nl}K_{nl}(x)dx - \int_{x_{cc}}^{x_{CBM}} \frac{x - x_{cc}}{x_{cc} - x_{CBM}} \beta_{nl}K_{nl}(x)dx, \quad (10)$$

which are calculated from the rotational kernel profiles (cf. Fig 18). The measured frequency splittings $\Delta f_p, \Delta f_g$ are calculated by averaging the splittings between each azimuthal order.

To determine the two unknowns $\Omega_{cc}, \Omega_{env}$ we only need a g- and a p-mode multiplet[6]. Optimally these should probe the extremities of the regions of concern. Based on Fig. 18 we choose the $g_1(\ell = 2)$ and $p_4(\ell = 1)$ multiplets which probe the near-core and envelope regions, respectively. For the $g_1(\ell = 2)$ multiplet we again choose the right-most frequencies in the observed doublets.

We collect all input information in Table 8. The K_0 values show that the p-mode multiplet is barely sensitive to the core and core-boundary mixing regions but that the g-mode multiplet has probing power. This can also be seen in Panel c) of Fig. 19, where the rotation kernel is non-zero in the core and near-core regions. Solving the system of two equations in Eq. (7) using the values in Table 8 yields $\Omega_{cc}/2\pi = 1.460$ d^{-1} and $\Omega_{env}/2\pi = 0.176$ d^{-1} for the two unknowns. Thus, the core region is rotating approximately 8.3 times faster than the envelope. We plot the resulting rotation profile in Panel d) of Fig. 19. The degree of differential rotation remains the same order of magnitude within our derived confidence interval, see Appendix E.

The envelope rotation frequency $\Omega_{env}/2\pi = 0.176$ d^{-1} derived using the three-zone model is approximately compatible with the frequency found in the TESS data, $f_{15} = 0.09852(2)$ d^{-1}, providing strong supporting evidence that this is indeed a harmonic of the surface rotation frequency $f_{rot,surf} = 2 \cdot f_{15} = 0.19704(4)$ d^{-1}. We use this value together with the stellar radius from the best model ($R_\star = 9.5^{+1.2}_{-0.8}$ $R_\odot$) to estimate the equatorial surface velocity as $v_{eq} = (2\pi f_{rot}) \cdot R_\star = 97 \pm 10$ km s^{-1}. This value agrees with the projected surface rotation velocity derived from high-resolution spectroscopy, $v \sin i = 27^{+6}_{-8}$ km s^{-1}, indicating that HD 192575 has an inclination $i \sim 16 \pm 5°$. The estimated v_{eq} is about 19% of the best models' critical rotation velocity $v_c = \sqrt{GM_\star/R_\star} \approx 511$ km s^{-1}, which is relatively high compared to other β Cep stars. Furthermore it is approximately the limit where our 1D treatment of rotationally perturbed low radial-order modes is considered reliable, see Lignières et al. (2006) and Reese et al. (2006) for p modes and Ballot et al. (2010) for g modes. So while the first-order perturbutative method is useful for a first estimate of the core rotation rate, future studies of HD 192575 should consider higher-order perturbative (e.g. Saio 1981; Dziembowski & Goode 1992; Suárez et al. 2006) and non-perturbative methods (e.g. the TAR approximation for g modes, Unno et al. 1989; Bildsten et al. 1996; Lai 1997; Townsend 2003).

6. Summary

In this paper we used HERMES spectroscopy and TESS photometry to perform detailed forward asteroseismic modelling of the newly-discovered β Cep star HD 192575. We demonstrated that non-LTE models are necessary to fit the spectroscopic line profiles and derive the atmospheric parameters correctly. The photometric analysis revealed a surface rotation frequency from rotational modulation and several frequency multiplets which allowed us to identify their angular degree ℓ and azimuthal order m. By combining this information with the spectroscopic error box and seismic models we were able to perform the mode identification for four frequency multiplets. Two $\ell = 2$ multiplets occur in overlap which we interpreted as the star being close to an avoided crossing. One other multiplet is likely an $\ell = 4$ mode showing that high-degree modes $\ell > 2$ are detectable with TESS space mission photometry, albeit at low amplitudes.

[6] Using more multiplets leads to an overdetermined system in this approximation.

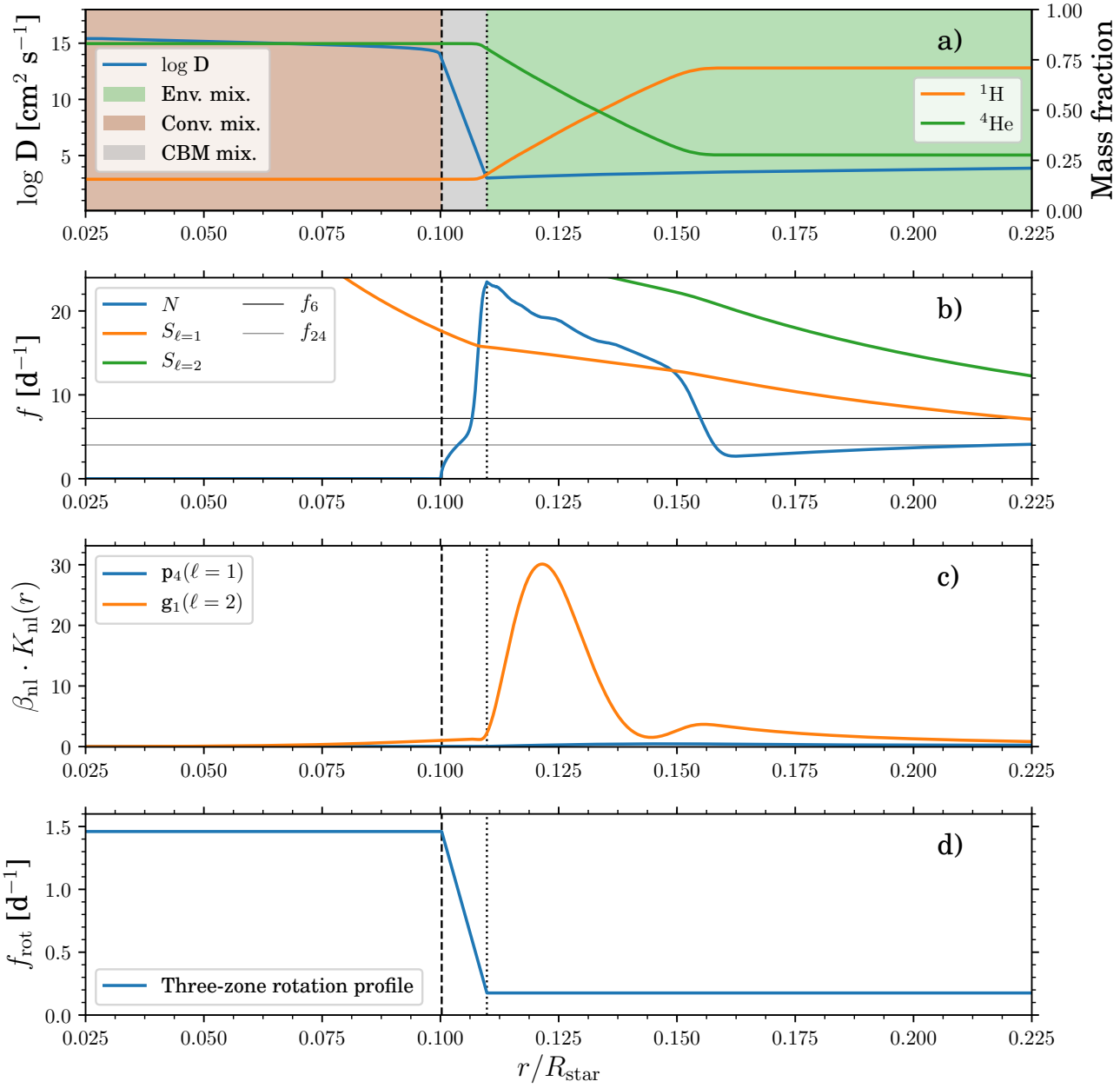

Fig. 19. Model properties and the three-zone rotation profile. Panel a) shows the mixing properties of the model, with the blue line indicating the level of mixing, the shaded regions different mixing regimes, and the orange and green lines the fractional mass of ^{1}H and ^{4}He respectively. Panel b) shows a propagation diagram, including the Brunt-Väisälä frequency N and the Lamb frequencies S_ℓ for $\ell = 1, 2$ as a function of the stellar radius. The zonal mode frequencies of the considered multiplets are shown as horizontal lines. Panel c) shows a zoom-in of the rotational kernel $\beta_{\rm nl} K_{\rm nl}$ as a function of the stellar radius. Panel d) shows the three-zone rotation profile as a function of the stellar radius as derived in the text. The vertical dashed and dotted lines on each panel are the core and core-boundary mixing boundaries, respectively.

Using the MESA stellar evolution and GYRE pulsation codes we determined tight constraints on the stellar mass $M_{\rm ini} = 13.0^{+3.5}_{-0.5}$ M$_\odot$ and age $t_{\rm age} = 14.1^{+1.7}_{-4.6}$ Myr which have confidence intervals that are comparable to those determined from eclipsing binaries in a similar mass regime. Varying the core boundary mixing parameter $f_{\rm CBM}$ allowed us to constrain the convective core mass of $M_{\rm cc} = 3.0^{+1.3}_{-0.3}$ M$_\odot$. We found that modelling results are relatively insensitive to the envelope mixing log $D_{\rm env}$ parameter, so future analysis of high-S/N spectra and abundances will help constrain this further. The best model has a radial $n_{\rm pg} = 0$ mode with a frequency of $f \sim 3.644$ d^{-1} which indicates that HD 192575 is both a multi-periodic p and g mode pulsator given the multiple frequencies detected in the low frequency regime, which makes it an interesting candidate for pulsation excitation studies (e.g. Daszyńska-Daszkiewicz et al. 2017). Our best standard-opacity model also does not predict the excitation of the observed p mode multiplets.

We performed a detailed study of the radial differential rotation from the rotationally-split frequency multiplets. Using a three-zone rotation model we were able to estimate that the near core rotates 8.3 times faster than the envelope. Such differentiality has been found in β Cep stars before, particularly ν Eridani (Pamyatnykh et al. 2004) and HD129929 (Dupret et al. 2004) but HD 192575 is the first β Cep star to have such a profile extracted with high precision in addition to tight constraints on mass, age and core mass using detailed forward asteroseismic modelling. This is in contrast to lower mass main-sequence stars with a convective core for which asteroseismic measurements tend to show more uniform radial rotation profiles (Van Reeth et al. 2018; Aerts et al. 2019). Instabilities due to the differential rotation can induce significant effects in the structure and future evolution of a massive star (Zahn 1992; Maeder & Meynet 2000; Maeder 2009), making HD192575 an important anchor in the study of interior rotation of massive stars. We plan a future study to perform a full rotational inversion analysis (e.g. Triana et al. 2015) by using more multiplets and moving beyond first-order perturbative methods, and to perform an abundance analysis of high-S/N spectra to derive further constraints on the envelope mixing.

Acknowledgements. The research leading to these results has received funding from the European Research Council (ERC) under the European Union's Horizon 2020 research and innovation program (grant agreement No. 670519: MAMSIE). DMB gratefully acknowledges a senior postdoctoral fellowship from the Research Foundation Flanders (FWO) with grant agreement no. 1286521N. MM gratefully acknowledges a PhD scholarship from the Research Foundation Flanders (FWO) under project No. 11F7120N. SS-D acknowledges support from the Spanish Government Ministerio de Ciencia e Innovación through grants PGC-2018-091 3741-B-C22, and from the Canarian Agency for Research, Innovation and Information Society (ACIISI), of the Canary Islands Government, and the European Regional Development Fund (ERDF), under grant with reference ProID2020010016. The MESA and GYRE developers are thanked for their efforts in providing, maintaining, and supporting the use of the open-source stellar-evolution code and pulsation codes. This research has made use of the SIMBAD database, operated at CDS, Strasbourg, France. Some/all of the data presented in this paper were obtained from the Mikulski Archive for Space Telescopes (MAST). STScI is operated by the Association of Universities for Research in Astronomy, Inc., under NASA contract NAS5-26555. The computational resources and services used in this work were provided by the VSC (Flemish Supercomputer Center), funded by the Research Foundation - Flanders (FWO) and the Flemish Government – department EWI.

Software: `MESA` (Paxton et al. 2011, 2013, 2015, 2018, 2019), `GYRE` (Townsend & Teitler 2013; Townsend et al. 2018; Goldstein & Townsend 2020).

Data processing & modelling: `Python 3.7` (Van Rossum & Drake 2009), including packages `numpy` (Oliphant 2006), `matplotlib` (Hunter 2007), `Pandas` (McKinney et al. 2010), and `lightkurve` (Lightkurve Collaboration et al. 2018).

References

Aerts, C. 2021, Reviews of Modern Physics, 93, 015001
Aerts, C., Briquet, M., Degroote, P., Thoul, A., & van Hoolst, T. 2011, A&A, 534, A98
Aerts, C., Christensen-Dalsgaard, J., & Kurtz, D. W. 2010, Asteroseismology (Springer)
Aerts, C. & De Cat, P. 2003, Space Sci. Rev., 105, 453
Aerts, C., De Cat, P., Handler, G., et al. 2004, MNRAS, 347, 463
Aerts, C., Mathis, S., & Rogers, T. M. 2019, ARA&A, 57, 35
Aerts, C., Molenberghs, G., Michielsen, M., et al. 2018, ApJS, 237, 15
Aerts, C., Simón-Díaz, S., Groot, P. J., & Degroote, P. 2014, A&A, 569, A118
Aerts, C., Thoul, A., Daszyńska, J., et al. 2003, Science, 300, 1926
Aizenman, M., Smeyers, P., & Weigert, A. 1977, A&A, 58, 41
Auvergne, M., Bodin, P., Boisnard, L., et al. 2009, A&A, 506, 411
Bailer-Jones, C. A. L., Rybizki, J., Fouesneau, M., Demleitner, M., & Andrae, R. 2021, AJ, 161, 147
Bailer-Jones, C. A. L., Rybizki, J., Fouesneau, M., Mantelet, G., & Andrae, R. 2018, AJ, 156, 58
Ballot, J., Lignières, F., Reese, D. R., & Rieutord, M. 2010, A&A, 518, A30
Banyard, G., Sana, H., Mahy, L., et al. 2021, arXiv e-prints, arXiv:2108.07814
Baran, A. S. & Koen, C. 2021, arXiv e-prints, arXiv:2106.09718
Baran, A. S., Koen, C., & Pokrzywka, B. 2015, MNRAS, 448, L16
Bildsten, L., Ushomirsky, G., & Cutler, C. 1996, ApJ, 460, 827
Björklund, R., Sundqvist, J. O., Puls, J., & Najarro, F. 2021, A&A, 648, A36
Bowman, D. M. 2017, Amplitude Modulation of Pulsation Modes in Delta Scuti Stars (Springer Theses series. ISBN 978-3-319-66649-5. Springer International Publishing)
Bowman, D. M. 2020, Frontiers in Astronomy and Space Sciences, 7, 70
Bowman, D. M. & Michielsen, M. 2021, arXiv e-prints, arXiv:2109.10776
Briquet, M., Aerts, C., Baglin, A., et al. 2011, A&A, 527, A112
Briquet, M., Morel, T., Thoul, A., et al. 2007, MNRAS, 381, 1482
Briquet, M., Neiner, C., Aerts, C., et al. 2012, MNRAS, 427, 483
Brott, I., Evans, C. J., Hunter, I., et al. 2011, A&A, 530, A116
Burssens, S., Simón-Díaz, S., Bowman, D. M., et al. 2020, A&A, 639, A81
Carneiro, L. P., Puls, J., Sundqvist, J. O., & Hoffmann, T. L. 2016, A&A, 590, A88
Carroll, J. A. 1933, MNRAS, 93, 478
Castelli, F. & Kurucz, R. L. 2003, in IAU Symposium, Vol. 210, Modelling of Stellar Atmospheres, ed. N. Piskunov, W. W. Weiss, & D. F. Gray, A20
Claret, A. & Torres, G. 2019, ApJ, 876, 134
Cristini, A., Meakin, C., Hirschi, R., et al. 2017, MNRAS, 471, 279
Daszyńska-Daszkiewicz, J., Pamyatnykh, A. A., Walczak, P., et al. 2017, MNRAS, 466, 2284
Davis, A., Jones, S., & Herwig, F. 2019, MNRAS, 484, 3921
Degroote, P., Briquet, M., Catala, C., et al. 2009, A&A, 506, 111
Dufton, P. L., Thompson, A., Crowther, P. A., et al. 2018, A&A, 615, A101
Dupret, M.-A., Thoul, A., Scuflaire, R., et al. 2004, A&A, 415, 251
Dziembowski, W. A. & Goode, P. R. 1992, ApJ, 394, 670
Dziembowski, W. A. & Pamyatnykh, A. A. 1991, A&A, 248, L11
Dziembowski, W. A. & Pamyatnykh, A. A. 2008, MNRAS, 385, 2061
Farmer, R., Fields, C. E., Petermann, I., et al. 2016, ApJS, 227, 22
Gaia Collaboration, Brown, A. G. A., Vallenari, A., et al. 2018, A&A, 616, A1
Gaia Collaboration, Brown, A. G. A., Vallenari, A., et al. 2021, A&A, 649, A1
Georgy, C., Ekström, S., Granada, A., et al. 2013, A&A, 553, A24
Georgy, C., Meynet, G., & Maeder, A. 2011, A&A, 527, A52
Gilet, C., Almgren, A. S., Bell, J. B., et al. 2013, ApJ, 773, 137
Goldstein, J. & Townsend, R. H. D. 2020, ApJ, 899, 116
Gray, D. F. 2005, The Observation and Analysis of Stellar Photospheres
Guetter, H. H. 1968, PASP, 80, 197
Handler, G., Jerzykiewicz, M., Rodríguez, E., et al. 2006, MNRAS, 365, 327
Handler, G., Pigulski, A., Daszyńska-Daszkiewicz, J., et al. 2019, ApJ, 873, L4
Handler, G., Shobbrook, R. R., & Mokgwetsi, T. 2005, MNRAS, 362, 612
Henyey, L., Vardya, M. S., & Bodenheimer, P. 1965, ApJ, 142, 841
Herwig, F. 2000, A&A, 360, 952
Higl, J., Müller, E., & Weiss, A. 2021, A&A, 646, A133
Higl, J. & Weiss, A. 2017, A&A, 608, A62
Hill, P. W. & Lynas-Gray, A. E. 1977, MNRAS, 180, 691
Hirschi, R., Meynet, G., & Maeder, A. 2004, A&A, 425, 649
Hohle, M. M., Neuhäuser, R., & Schutz, B. F. 2010, Astronomische Nachrichten, 331, 349
Horst, L., Edelmann, P. V. F., Andrássy, R., et al. 2020, A&A, 641, A18
Horst, L., Hirschi, R., Edelmann, P. V. F., Andrassy, R., & Roepke, F. K. 2021, arXiv e-prints, arXiv:2107.02199
Hunter, I., Brott, I., Langer, N., et al. 2009, A&A, 496, 841
Hunter, I., Brott, I., Lennon, D. J., et al. 2008, ApJ, 676, L29
Hunter, J. D. 2007, Computing in science & engineering, 9, 90
Jenkins, J. M., Twicken, J. D., McCauliff, S., et al. 2016, in Proc. SPIE, Vol. 9913, Software and Cyberinfrastructure for Astronomy IV, 99133E
Jerzykiewicz, M., Handler, G., Shobbrook, R. R., et al. 2005, MNRAS, 360, 619
Kaiser, E. A., Hirschi, R., Arnett, W. D., et al. 2020, MNRAS, 496, 1967
Keszthelyi, Z., Meynet, G., Georgy, C., et al. 2019, MNRAS, 485, 5843
Keszthelyi, Z., Puls, J., & Wade, G. A. 2017, A&A, 598, A4
Kippenhahn, R., Weigert, A., & Weiss, A. 2012, Stellar Structure and Evolution
Kurtz, D. W., Saio, H., Takata, M., et al. 2014, MNRAS, 444, 102
Lai, D. 1997, ApJ, 490, 847
Langer, N. 2012, ARA&A, 50, 107
Ledoux, P. 1951, ApJ, 114, 373
Lee, U. 2021, MNRAS, 505, 1495
Lightkurve Collaboration, Cardoso, J. V. d. M., Hedges, C., et al. 2018, Lightkurve: Kepler and TESS time series analysis in Python, Astrophysics Source Code Library
Lignières, F., Rieutord, M., & Reese, D. 2006, A&A, 455, 607
Lomb, N. R. 1976, Ap&SS, 39, 447
Loumos, G. L. & Deeming, T. J. 1978, Ap&SS, 56, 285
Maeder, A. 2009, Physics, Formation and Evolution of Rotating Stars (Springer Berlin Heidelberg)
Maeder, A. & Meynet, G. 2000, ARA&A, 38, 143
Maitre, V. 1965, Journal des Observateurs, 48, 45
Martins, F., Simón-Díaz, S., Barbá, R. H., Gamen, R. C., & Ekström, S. 2017, A&A, 599, A30

Mazumdar, A., Briquet, M., Desmet, M., & Aerts, C. 2006, A&A, 459, 589
McEvoy, C. M., Dufton, P. L., Evans, C. J., et al. 2015, A&A, 575, A70
McKinney, W. et al. 2010, in Proceedings of the 9th Python in Science Conference, Vol. 445, Austin, TX, 51–56
Meakin, C. A. & Arnett, D. 2007, ApJ, 667, 448
Michielsen, M., Aerts, C., & Bowman, D. M. 2021, A&A, 650, A175
Miglio, A., Montalbán, J., & Dupret, M.-A. 2007a, MNRAS, 375, L21
Miglio, A., Montalbán, J., & Dupret, M.-A. 2007b, Communications in Asteroseismology, 151, 48
Mombarg, J. S. G., Van Reeth, T., & Aerts, C. 2021, Astronomy and astrophysics (Berlin), 650, A58
Morel, T., Butler, K., Aerts, C., Neiner, C., & Briquet, M. 2006, A&A, 457, 651
Moya, A., Christensen-Dalsgaard, J., Charpinet, S., et al. 2008, Ap&SS, 316, 231
Nieva, M. F. & Przybilla, N. 2007, A&A, 467, 295
Nieva, M. F. & Przybilla, N. 2012, A&A, 539, A143
Oja, T. 1991, A&AS, 89, 415
Oliphant, T. E. 2006, A guide to NumPy, Vol. 1 (Trelgol Publishing USA)
Pamyatnykh, A. A. 1999, Acta Astron., 49, 119
Pamyatnykh, A. A., Handler, G., & Dziembowski, W. A. 2004, MNRAS, 350, 1022
Pápics, P. I., Briquet, M., Baglin, A., et al. 2012, A&A, 542, A55
Pápics, P. I., Tkachenko, A., Van Reeth, T., et al. 2017, A&A, 598, A74
Paxton, B., Bildsten, L., Dotter, A., et al. 2011, ApJS, 192, 3
Paxton, B., Cantiello, M., Arras, P., et al. 2013, ApJS, 208, 4
Paxton, B., Marchant, P., Schwab, J., et al. 2015, ApJS, 220, 15
Paxton, B., Schwab, J., Bauer, E. B., et al. 2018, ApJS, 234, 34
Paxton, B., Smolec, R., Schwab, J., et al. 2019, ApJS, 243, 10
Pedersen, M. G., Aerts, C., Pápics, P. I., et al. 2021, Nature Astronomy, 5, 715
Pedersen, M. G., Aerts, C., Pápics, P. I., & Rogers, T. M. 2018, A&A, 614, A128
Pedersen, M. G., Chowdhury, S., Johnston, C., et al. 2019, ApJ, 872, L9
Pols, O. R., Tout, C. A., Schroder, K.-P., Eggleton, P. P., & Manners, J. 1997, MNRAS, 289, 869
Puls, J., Najarro, F., Sundqvist, J. O., & Sen, K. 2020, A&A, 642, A172
Puls, J., Sundqvist, J. O., & Markova, N. 2015, in IAU Symposium, Vol. 307, New Windows on Massive Stars, ed. G. Meynet, C. Georgy, J. Groh, & P. Stee, 25–36
Puls, J., Urbaneja, M. A., Venero, R., et al. 2005, A&A, 435, 669
Ramírez-Agudelo, O. H., Simón-Díaz, S., Sana, H., et al. 2013, A&A, 560, A29
Raskin, G., van Winckel, H., Hensberge, H., et al. 2011, A&A, 526, A69
Reese, D., Lignières, F., & Rieutord, M. 2006, A&A, 455, 621
Ricker, G. R., Winn, J. N., Vanderspek, R., et al. 2015, Journal of Astronomical Telescopes, Instruments, and Systems, 1, 014003
Rivero González, J. G., Puls, J., Najarro, F., & Brott, I. 2012, A&A, 537, A79
Rogers, T. M. & McElwaine, J. N. 2017, ApJ, 848, L1
Saio, H. 1981, ApJ, 244, 299
Salaris, M. & Cassisi, S. 2017, Royal Society Open Science, 4, 170192
Santolaya-Rey, A. E., Puls, J., & Herrero, A. 1997, A&A, 323, 488
Scargle, J. D. 1982, ApJ, 263, 835
Seaton, M. J. 2005, MNRAS, 362, L1
Simón-Díaz, S. 2010, A&A, 510, A22
Simón-Díaz, S., Godart, M., Castro, N., et al. 2017, A&A, 597, A22
Simón-Díaz, S. & Herrero, A. 2014, A&A, 562, A135
Simón-Díaz, S., Herrero, A., Esteban, C., & Najarro, F. 2006, A&A, 448, 351
Southworth, J., Bowman, D. M., & Pavlovski, K. 2021, MNRAS, 501, L65
Southworth, J., Bowman, D. M., Tkachenko, A., & Pavlovski, K. 2020, MNRAS, 497, L19
Stankov, A. & Handler, G. 2005, ApJS, 158, 193
Suárez, J. C., Goupil, M. J., & Morel, P. 2006, A&A, 449, 673
Sundqvist, J. O. & Puls, J. 2018, A&A, 619, A59
Tkachenko, A. 2015, A&A, 581, A129
Tkachenko, A., Pavlovski, K., Johnston, C., et al. 2020, A&A, 637, A60
Townsend, R. H. D. 2003, MNRAS, 340, 1020
Townsend, R. H. D., Goldstein, J., & Zweibel, E. G. 2018, MNRAS, 475, 879
Townsend, R. H. D., Rivinius, T., Rowe, J. F., et al. 2013, ApJ, 769, 33
Townsend, R. H. D. & Teitler, S. A. 2013, MNRAS, 435, 3406
Triana, S. A., Moravveji, E., Pápics, P. I., et al. 2015, ApJ, 810, 16
Tsymbal, V. 1996, in Astronomical Society of the Pacific Conference Series, Vol. 108, M.A.S.S., Model Atmospheres and Spectrum Synthesis, ed. S. J. Adelman, F. Kupka, & W. W. Weiss, 198
Unno, W., Osaki, Y., Ando, H., Saio, H., & Shibahashi, H. 1989, Nonradial oscillations of stars
Van Beeck, J., Bowman, D. M., Pedersen, M. G., et al. 2021, arXiv e-prints, arXiv:2108.02907
Van Reeth, T., Mombarg, J. S. G., Mathis, S., et al. 2018, A&A, 618, A24
Van Rossum, G. & Drake, F. L. 2009, Python 3 Reference Manual (Scotts Valley, CA: CreateSpace)
Vink, J. S., de Koter, A., & Lamers, H. J. G. L. M. 2001, A&A, 369, 574
Walczak, P., Daszyńska-Daszkiewicz, J., Pigulski, A., et al. 2019, MNRAS, 485, 3544
Walczak, P., Fontes, C. J., Colgan, J., Kilcrease, D. P., & Guzik, J. A. 2015, A&A, 580, L9
Walker, G., Matthews, J., Kuschnig, R., et al. 2003, PASP, 115, 1023
Weiss, W. W., Rucinski, S. M., Moffat, A. F. J., et al. 2014, PASP, 126, 573
Weiss, W. W., Zwintz, K., Kuschnig, R., et al. 2021, Universe, 7, 199
Wilson, R. E. 1953, Carnegie Institute Washington D.C. Publication, 0
Zahn, J. P. 1992, A&A, 265, 115

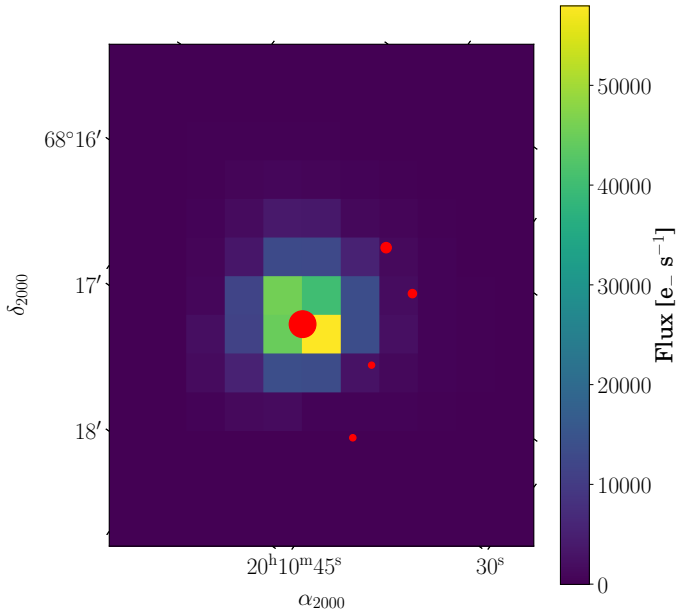

Fig. A.1. Pixel map of the first frame of the target pixel frame of sector 15 of HD 192575. The colour of each pixel indicates the the total flux. The red markers indicate sources obtained from the Gaia-DR2 catalogue. Their size is scaled by their mean Gaia G-band magnitude ranging between $G_{\rm Gaia} = 6.78$ mag for the central source, and $G_{\rm Gaia} \in [15.44, 16.46]$ mag for the other nearby sources.

Appendix A: TESS aperture mask

In this section we present the TESS aperture mask of HD 192575 in Fig. A.1. We find a clear central source where the majority of the flux comes from. We find four nearby sources marked in red, notably dimmer in magnitude. The difference in magnitude between these sources and the bright central source is significant enough to disregard them as possible source of contamination in the light curve extraction.

Appendix B: Full frequency lists

In this section we present the complete frequency list resulting from the analysis in Section 3.2. In total we find 79 frequencies given in Table E.3. The first column assigns a unique identification number to the frequency. The second through fourth column give the frequency, amplitude and phase values of the frequency with the error on the last digit given between brackets. The last column contains notes about the particular frequency (e.g multiplet membership or rotational modulation).

Appendix C: MESA and GYRE inlists

Example MESA and GYRE inlists are available on the MESA inlist section of the MESA Marketplace: `http://cococubed.asu.edu/mesa_market/inlists.html` [To be uploaded].

Appendix D: Radial order fitting

The radial order fitting strategy was described in Section 4.2. We used a combination of mode evolution diagrams (e.g. Fig. 9) and best model plots by fixing certain frequencies (e.g. Fig. 8 and Fig. 10). A summarising diagram of the selection process is given in Fig. D.1, which ultimately led to three possible mode configurations. Only mode configuration A provides a possible explanation of the observed bifurcations and was therefore favoured in the main text. In this appendix we include all intermediate diagnostic diagrams used to construct the three mode configurations here.

Appendix D.1: Fitting trip1

We found in Section 4.2.1 that the dominant multiplet (quad1; f_3, f_2, f_5, f_4) can be fit as an $\ell = 2$ with three different radial orders possible within the 3σ spectroscopic constraints. We proceeded by fixing f_2 as the zonal frequency for the different radial orders ($n_{\rm p} = 0, 1, 2$). The $n_{\rm pg} = 0$ case was shown in Fig. 10 which allowed us to fix the radial order of the triplet containing the dominant multiplet (trip1; f_{56}, f_6, f_1) as a $\ell = 1, n_{\rm pg} = 2$. We show the results for radial orders $n_{\rm pg} = 1$ and $n_{\rm pg} = 2$ in Fig. D.2 and Fig. D.3 respectively. We find that the triplet is confirmed as $\ell = 1$ with increased radial order (cf. Fig. D.1).

Appendix D.2: Fitting quint1

We found in Section 4.2.1 that the bifurcations of quint1 cannot be explained in mode configurations B and C. That is, only one possible configuration (a g_2 mode) was found in the frequency range of quint1 that would also reproduce the other multiplets. We show this in Fig. D.4 and Fig. D.5 for mode configuration C and B, respectively. Mode configuration B does show a close $g_1(\ell = 2)$ mode but fitting it in this configuration did not reproduce the other multiplets. In the case of mode configuration A we considered the overlap of two $\ell = 2$ modes (with a potential third $\ell = 1$ mode, cf. Section 4.2.3) since for this configuration the star is near an avoided crossing, see Fig. D.6.

Appendix E: Deriving rotation from the multiplets

Appendix E.1: Rigid rotation models

In this section we elaborate on the derivation of the stellar rotation frequency from the observed multiplets and the rigid rotation assumption, Eq. (2), discussed in Section 5. For each multiplet consisting of N non-zonal frequencies we calculate the non-zonal frequencies $f_{n\ell m}$ using Eq. (2), the observed $f_{\rm n0l}$, the $\beta_{\rm nl}$ constant from the best model, and a range of rotation frequencies $f_{\rm rot} \in [f_{\rm rot,low}, f_{\rm rot,high}]$. We then calculate the reduced χ^2 value for each $f_{\rm rot}$ value by summing over the N non-zonal frequencies as

$$\chi^2_{\rm red} = \frac{1}{N_{\rm obs} - k} \sum_{i=1}^{N} \left(\frac{f^i_{\rm obs} - f^i_{\rm theo}}{f_{\rm res}} \right)^2, \tag{E.1}$$

where $N_{\rm obs}$ is the number of non-zonal modes, $k = 1$ the number of free parameters to estimate ($f_{\rm rot}$), $f^i_{\rm obs}$ the observed non-zonal frequency, $f^i_{\rm theo}$ the calculated non-zonal frequency, and $f_{\rm res} = 0.00308$ d^{-1} the frequency resolution of the light curve. We show the results of this exercise for multiplet quad1 (consisting of three non-zonal frequencies) in Fig. E.1. The stellar model is the model derived in Section 4.3. In this case we consider a range $f_{\rm rot} \in [0.05, 0.035]$ d^{-1} in 300 steps. A clear minimum is reached with a 3σ confidence interval given by the blue horizontal line. This confidence interval is defined as

$$\chi^2_{3\sigma} = \frac{\chi^2_{3\sigma,w} \cdot \chi^2_{\rm red,min}}{w}, \tag{E.2}$$

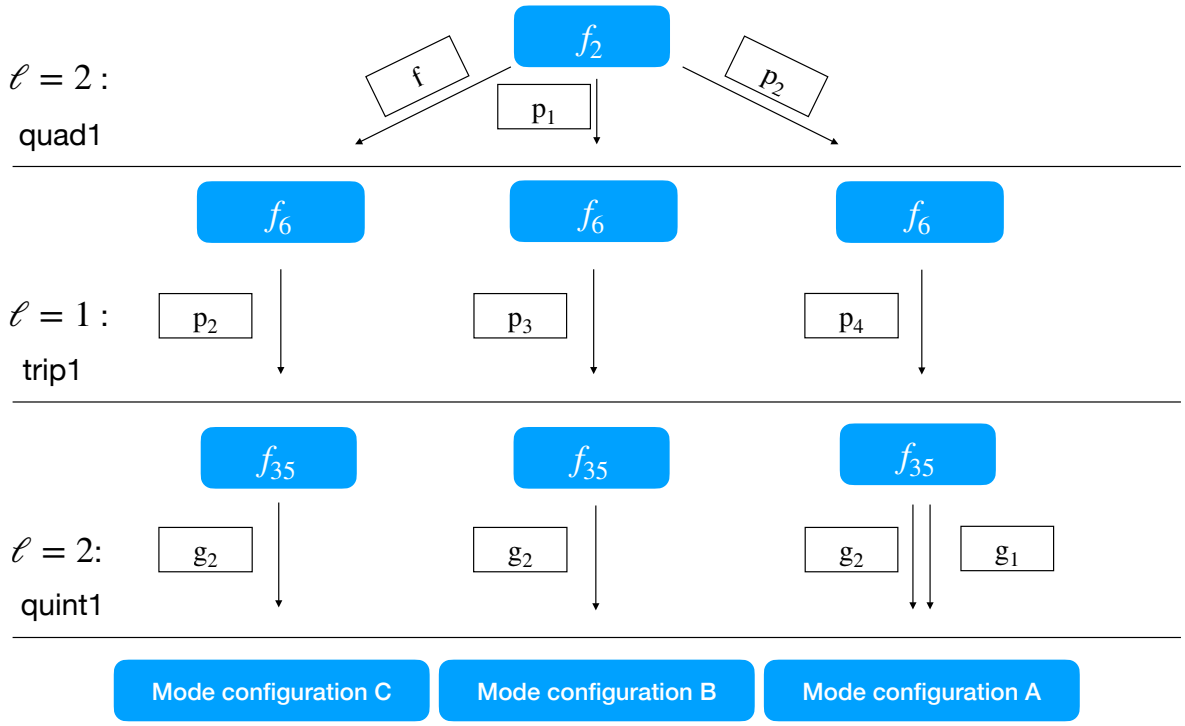

Fig. D.1. Tree diagram of the radial order fitting sequence. We start from the dominant quadruplet quad1 with f_2 as the zonal mode which can be fitted as three radial orders within the 3σ spectroscopic error box. This generates three configuration branches, which are pursued to fix the other multiplets. This leads to the three mode configurations described in the text. Note that mode configuration A is a special case as quint1 is fitted as two overlapping $\ell = 2$ modes (see text for details).

where $\chi^2_{\mathrm{red,min}}$ is the χ^2 value of the best fit, $w = N_{\mathrm{obs}} - 1$ the degrees of freedom and $\chi^2_{1\sigma,w}$ is the tabulated value of the 3σ confidence interval of the cumulative distribution function of a χ^2 distribution with w degrees freedom. In the above example, $w = 3 - 1 = 2$, and $\chi^2_{3\sigma,2} = 11.83$. By calculating the intersection of $\chi^2_{3\sigma}$ with a fit through the χ^2 distribution we obtain a confidence interval on the derived rotation frequency. We also show the theoretical frequencies obtained for this optimised rotation frequency in Fig. E.2.

Appendix E.1.1: Choice of frequencies in quint1

In Section 5 we assumed that the left frequencies in the doublets in the quint1 multiplet belong to the $g_2(\ell = 2)$ mode (quint1a) and the right frequencies to the $g_1(\ell = 2)$ mode (quint1b). Here we show that the particular choice of frequencies has little effect on the derived frequency in the rigid rotation approximation. The possible combinations of frequencies is shown in Table E.1. The combination used in the main text is shown on the first row. From the table it becomes clear that the specific frequency choice does not change the derived rotation frequency within 3σ, and that this derived rotation frequency is clearly higher than the rotation frequencies derived from the higher frequency multiplets (cf. Section 5).

Table E.1. Derived rigid rotation frequency f_{rot} for all possible frequency configurations in the overlapping multiplet quint1. The first column and second column show the frequencies in the lower frequency multiplet (g_2, quint1a) and the higher frequency multiplet (g_1, quint1b), respectively. The last column shows the derived rotation frequency for each case with the 3σ error on the last digit.

quint1a	quint1b	$f_{\mathrm{rot,a}}/f_{\mathrm{rot,b}}$ [d^{-1}]
$(f_{26}, f_{25}, f_{33}, f_{24})$	$(f_{19}, f_{35}, f_{24}, f_{48})$	0.23(2)/0.21(2)
$(f_{26}, f_{19}, f_{35}, f_{24})$	$(f_{25}, f_{33}, f_{24}, f_{48})$	0.23(2)/0.23(3)
$(f_{26}, f_{25}, f_{35}, f_{24})$	$(f_{19}, f_{33}, f_{24}, f_{48})$	0.24(3)/0.23(3)
$(f_{26}, f_{19}, f_{33}, f_{24})$	$(f_{25}, f_{35}, f_{24}, f_{48})$	0.23(2)/0.22(2)

Appendix E.2: Three-zone model

In this section we gauge the sensitivity of the derived differential rotation with regards to different models. We select four additional models shown in Table E.2. The first model is the best model derived in Section 4.3. The second and third model are models at the hot and cool extremities of the derived confidence interval. The fourth and fifth model are the same model as the best model but with a different $\log D_{\mathrm{env}}$. We estimate the rotation profile for each of these models following the method in

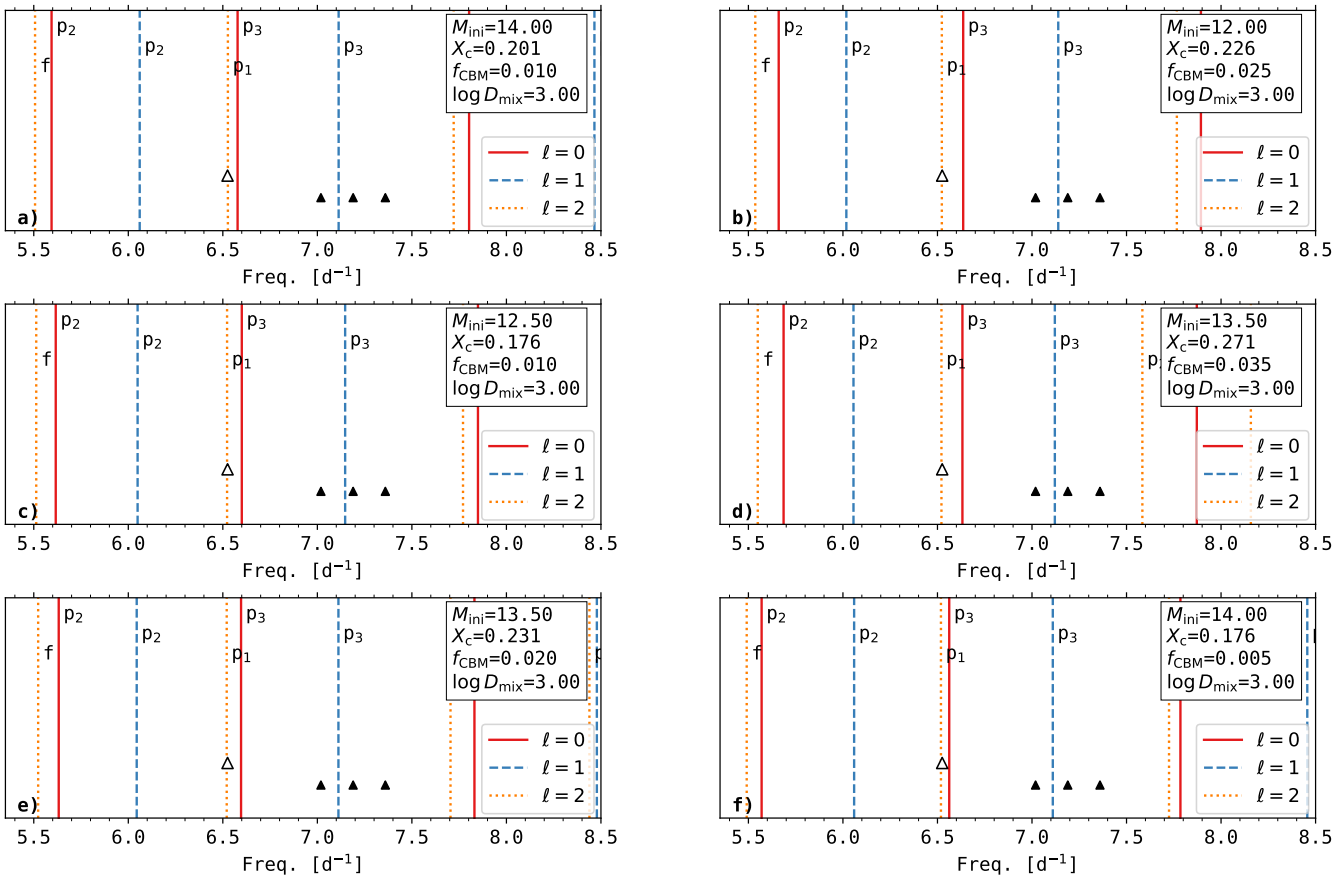

Fig. D.2. Best models assuming f_2 is an $(\ell, n_{pg}) = (2, 1)$ zonal mode in the 3σ spectroscopic error box. Same layout as Fig. 10. The fitted frequency (f_2) is given by an empty triangle while the dark triangles indicated the non-fitted triplet frequencies (f_{56}, f_6, f_1).

Table E.2. Stellar models considered for the derivation of the three-zone rotation profile. The model properties are given in the first four columns. The derived rotation rates are given in the fifth and sixth column. The last column gives the degree of differential rotation between the core and envelope.

M_{ini}	f_{CBM}	log D_{env}	X_c	$\Omega_{cc}/2\pi$	$\Omega_{env}/2\pi$	Ω_{cc}/Ω_{env}
[M$_\odot$]		[dex]		[d^{-1}]	[d^{-1}]	
13.00	0.020	3.00	0.156	1.460	0.176	8.3
12.50	0.030	3.00	0.206	2.147	0.174	12.3
16.00	0.005	3.00	0.111	1.273	0.177	7.2
13.00	0.020	2.00	0.156	1.430	0.176	8.1
13.00	0.020	4.00	0.156	1.509	0.176	8.6

Section 5. The selected modes are again $g_1(\ell = 2)$ and $p_4(\ell = 1)$, except for the 12 M$_\odot$ model where we select the $g_2(\ell = 2)$ as in this case it has higher probing power relative to the $g_1(\ell = 2)$ mode.

We find that the degree of differential rotation remains the same order of magnitude, as seen in the last column of Table E.2. The envelope rotation rates are similar indicating that the p-mode multiplets provide a quasi model-independent estimate of the envelope rotation rate in this temperature regime. The core rotation rates are more model dependent. More specifically on the mixing properties, parameterised by f_{CBM} and log D_{env}, with higher mixing increasing the degree of differential rotation.

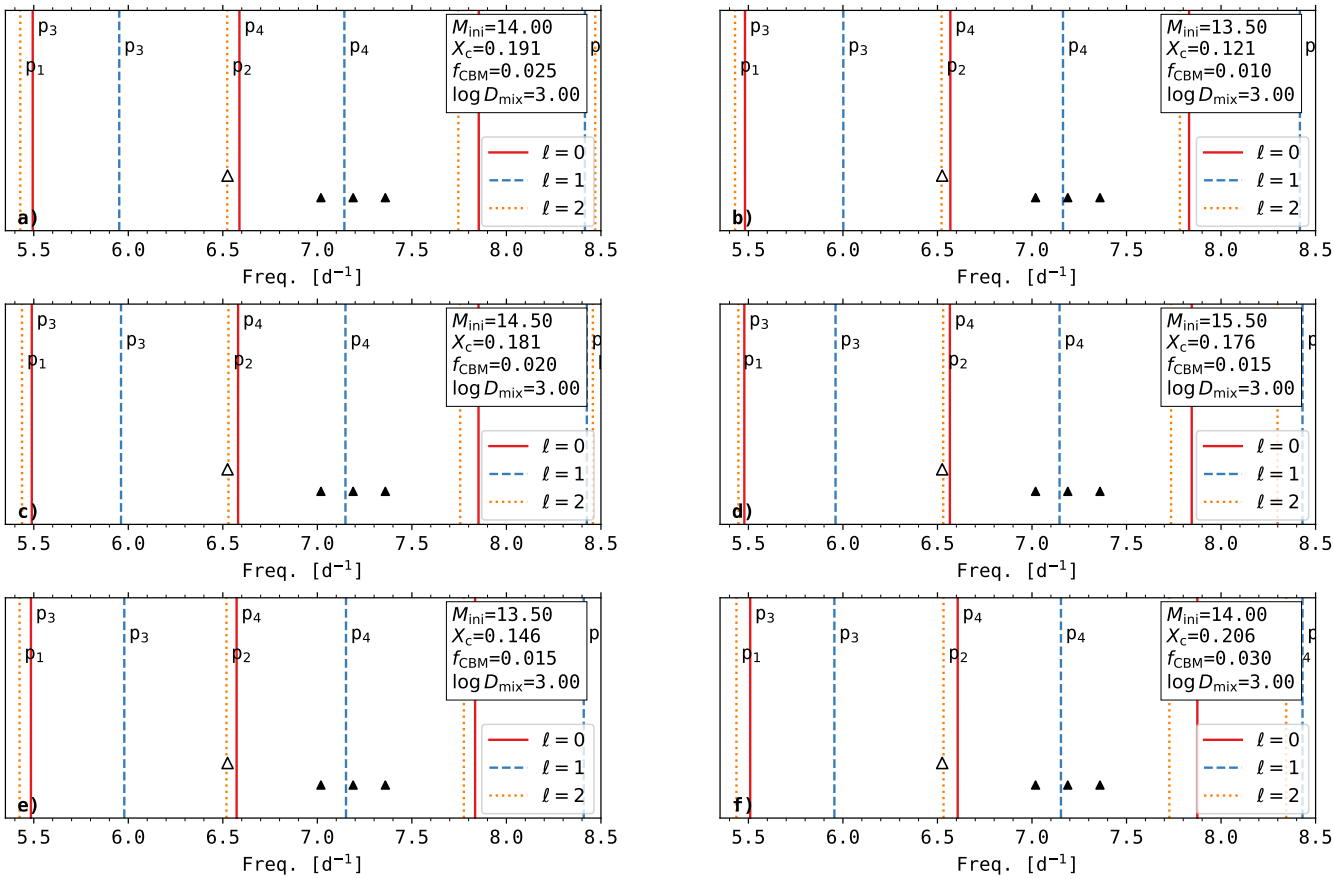

Fig. D.3. Best models assuming f_2 is an $(\ell, n_{pg}) = (2, 2)$ zonal mode in the 3σ spectroscopic error box. Same layout as Fig. 10. The fitted frequency (f_2) is given by an empty triangle while the dark triangles indicated the non-fitted triplet frequencies (f_{56}, f_6, f_1).

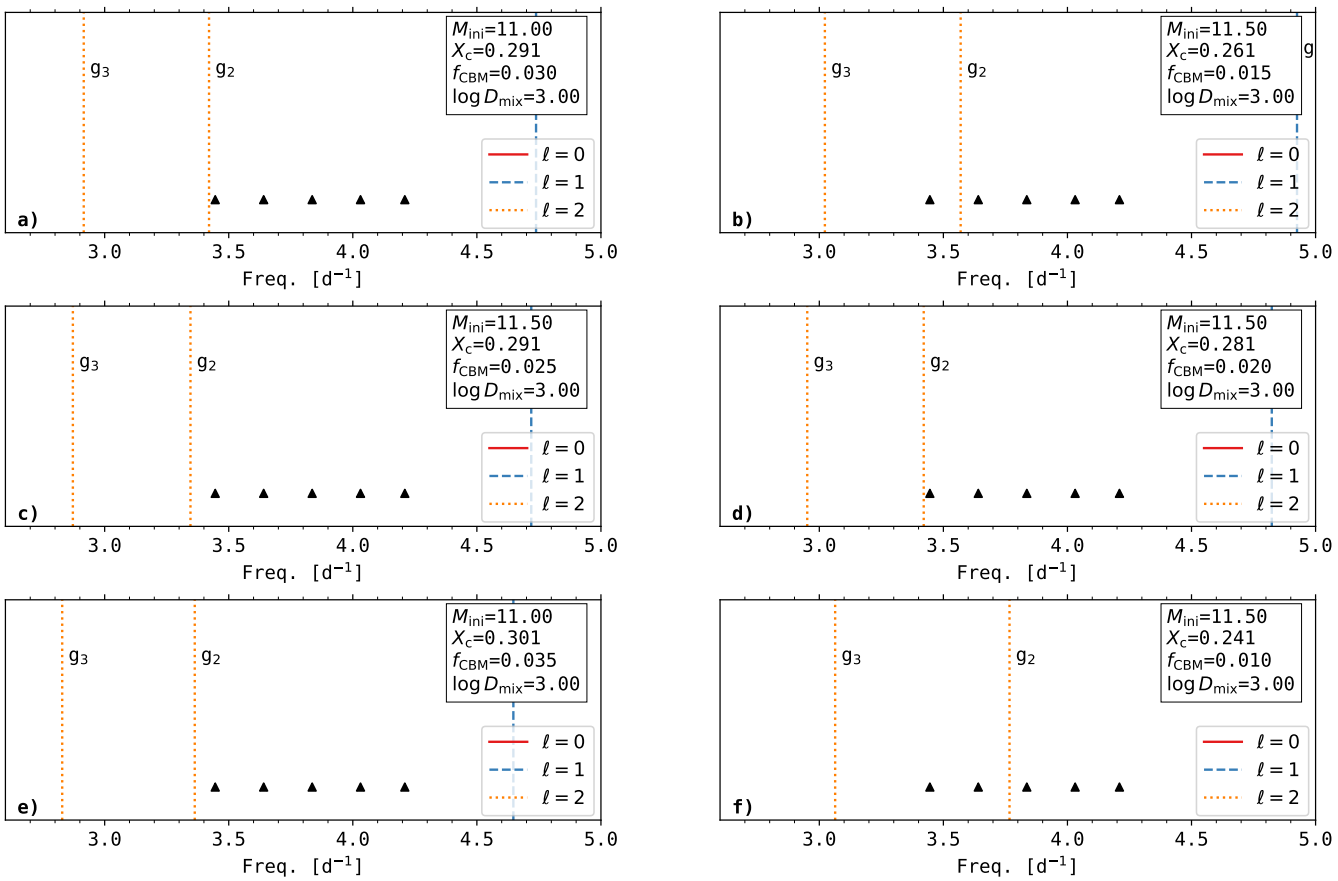

Fig. D.4. Best models assuming f_2 as an $(\ell, n_{pg}) = (2, 0)$ zonal mode and f_6 as a $(\ell, n_{pg}) = (1, 2)$ zonal mode (mode configuration C in the text). Same layout as in Fig. 10. Fitted frequencies f_2 and f_6 are not shown in order to visualise the possible radial orders for the quint1 multiplet ($f_{26}, f_{19}, f_{35}, f_{24}, f_{48}$, as black triangles).

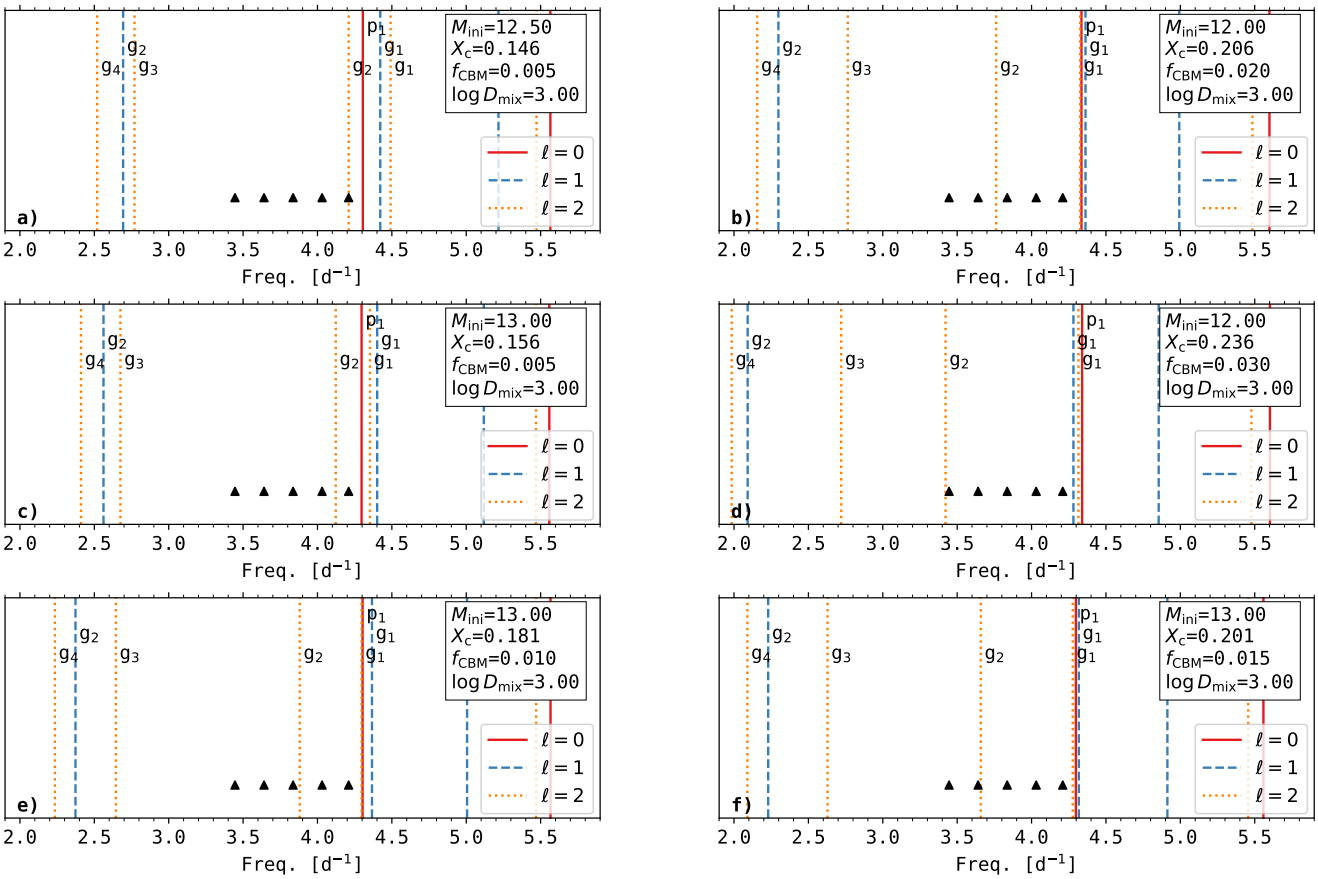

Fig. D.5. Best models assuming f_2 as an $(\ell, n_{pg}) = (2, 1)$ zonal mode and f_6 as a $(\ell, n_{pg}) = (1, 3)$ zonal mode (mode configuration B in the text). Same layout as in Fig. 10. Fitted frequencies f_2 and f_6 are not shown in order to visualise the possible radial orders for the quint1 multiplet ($f_{26}, f_{19}, f_{35}, f_{24}, f_{48}$, as black triangles).

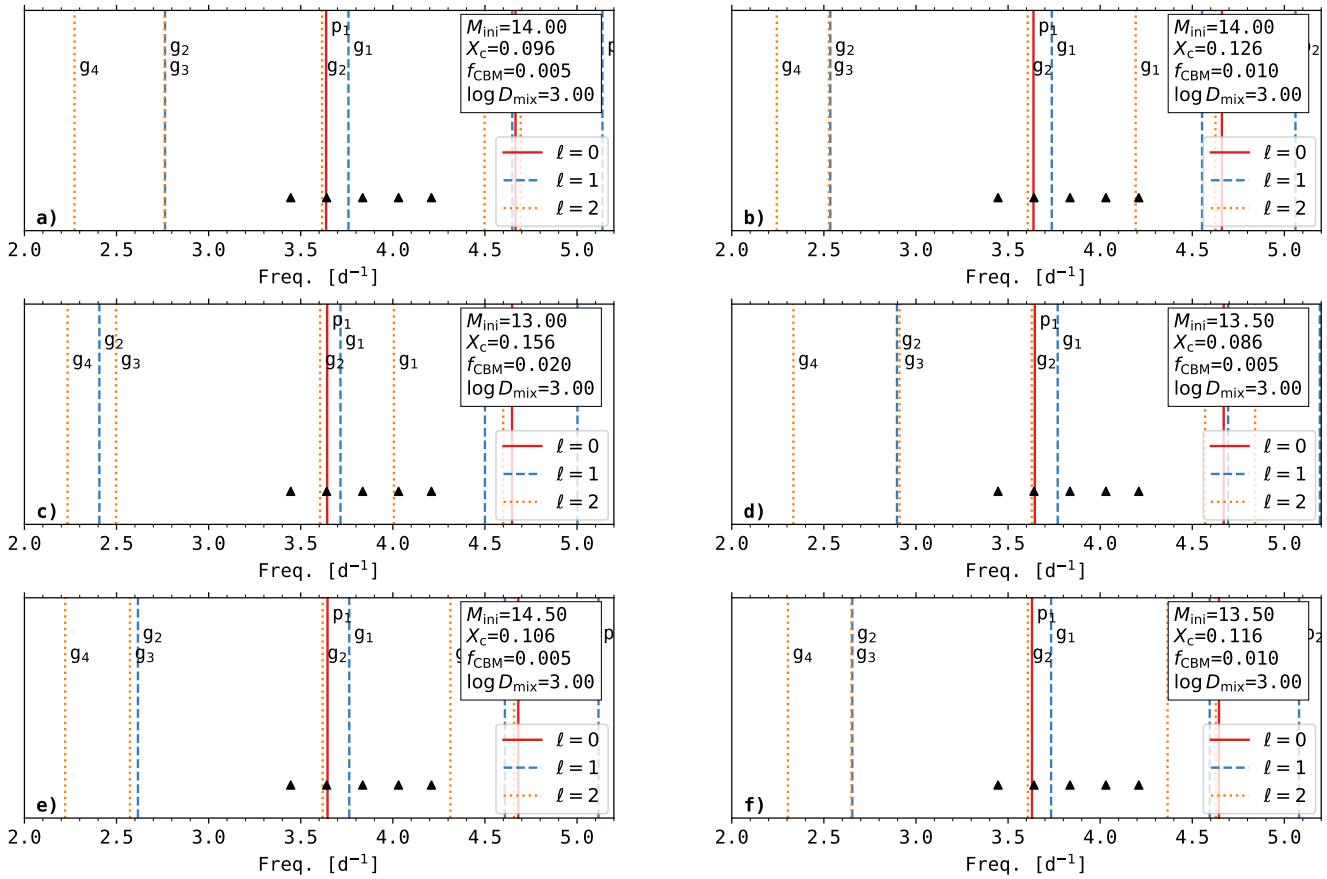

Fig. D.6. Best models assuming f_2 as an $(\ell, n_{\rm pg}) = (2, 2)$ zonal mode and f_6 as a $(\ell, n_{\rm pg}) = (1, 4)$ zonal mode (mode configuration A in the text). Same layout as in Fig. 10. Fitted frequencies f_2 and f_6 are not shown in order to visualise the possible radial orders for the quint1 multiplet ($f_{26}, f_{19}, f_{35}, f_{24}, f_{48}$, as black triangles).

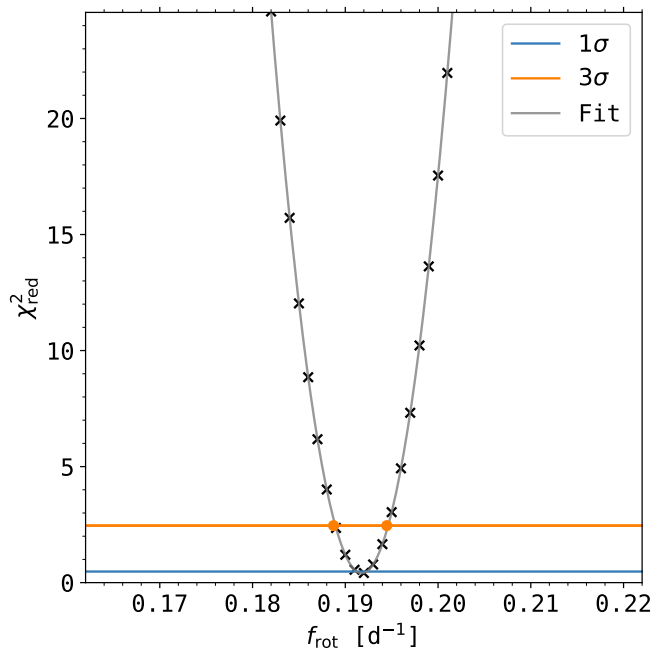

Fig. E.1. χ^2 distribution when fitting quad1 with different rotation frequencies. Each χ^2 value is marked with a black cross. The 1σ and 3σ confidence intervals are given by blue and orange lines respectively. A polynomial fit through the data points is given grey. The edges of the 3σ confidence interval are given by orange dots.

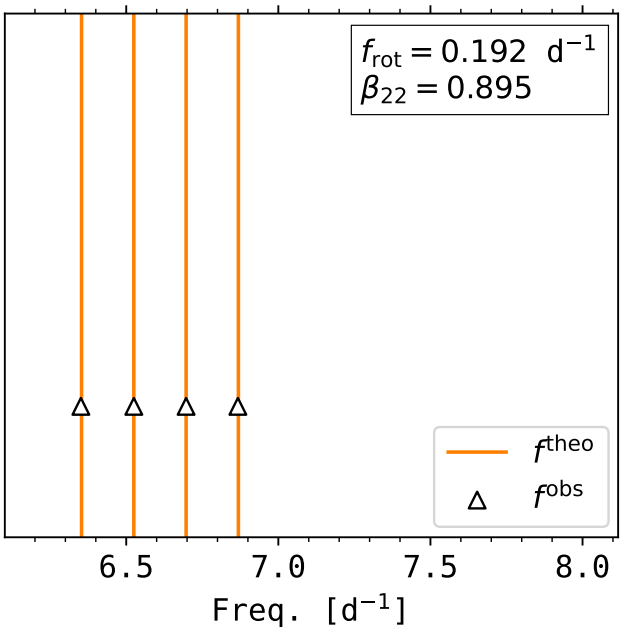

Fig. E.2. Theoretical fit to the quad1 multiplet when using the rotation frequency derived from the χ^2 analysis.

Table E.3. Full frequency list of HD192575.

id.	Frequency (d^{-1})	Amplitude (mmag)	Phase (rad)	Notes
f_1	7.359625(1)	3.485(3)	1.2683(7)	trip1
f_2	6.525005(2)	2.453(3)	0.494(1)	quad1
f_3	6.350919(2)	1.988(3)	2.676(1)	quad1
f_4	6.867008(4)	0.900(3)	2.202(3)	quad1
f_5	6.696791(5)	0.751(3)	-1.182(3)	quad1
f_6	7.189246(8)	0.518(3)	-2.263(5)	trip1
f_7	8.96669(1)	0.417(3)	-2.671(6)	
f_8	6.46341(1)	0.379(3)	-0.196(7)	quad2
f_9	7.10093(1)	0.327(3)	-0.631(8)	
f_{10}	7.95372(1)	0.290(3)	-0.702(9)	doub1
f_{11}	1.35501(2)	0.258(3)	-3.08(1)	
f_{12}	6.68272(2)	0.246(3)	2.82(1)	quad2
f_{13}	6.29283(2)	0.246(3)	-0.75(1)	quad2
f_{14}	6.11813(2)	0.236(3)	-2.39(1)	quad2
f_{15}	0.09852(2)	0.211(3)	-1.20(1)	$0.5f_{\rm rot}$
f_{16}	7.47607(2)	0.203(3)	1.48(1)	trip2
f_{17}	6.63072(2)	0.187(3)	-2.42(1)	
f_{18}	7.64721(2)	0.168(3)	-3.08(1)	trip2
f_{19}	3.64072(3)	0.130(3)	-2.44(2)	
f_{20}	9.19716(4)	0.108(3)	-1.14(2)	
f_{21}	11.20563(4)	0.111(3)	-1.65(2)	
f_{22}	1.63748(4)	0.113(3)	-0.57(2)	doub2
f_{23}	12.99982(4)	0.102(3)	2.41(2)	
f_{24}	4.03104(4)	0.105(3)	1.36(2)	
f_{25}	3.62488(4)	0.093(3)	-0.40(3)	
f_{26}	3.44556(4)	0.108(3)	0.96(2)	
f_{27}	1.19238(5)	0.085(3)	0.61(3)	
f_{28}	1.83767(4)	0.089(3)	-2.78(3)	doub3
f_{29}	9.54270(5)	0.079(3)	3.12(3)	quint2
f_{30}	7.78074(5)	0.076(3)	2.74(3)	doub1
f_{31}	10.03443(6)	0.071(3)	2.13(4)	quint2
f_{32}	3.06142(6)	0.068(3)	2.51(4)	
f_{33}	3.81867(6)	0.068(3)	2.05(4)	
f_{34}	2.98535(6)	0.064(3)	-2.33(4)	
f_{35}	3.83624(6)	0.062(3)	1.29(4)	
f_{36}	6.77961(7)	0.060(3)	-2.31(4)	
f_{37}	9.31029(7)	0.058(3)	3.05(4)	quint2
f_{38}	4.85127(7)	0.056(3)	-2.72(4)	
f_{39}	7.70588(7)	0.056(3)	-0.74(5)	

Table E.3. continued.

id.	Frequency (d^{-1})	Amplitude (mmag)	Phase (rad)	Notes
f_{40}	9.78958(7)	0.054(3)	-1.10(5)	quint2
f_{41}	8.99672(7)	0.057(3)	-2.43(4)	
f_{42}	6.59172(8)	0.053(3)	2.82(5)	
f_{43}	2.39685(7)	0.054(3)	0.53(5)	
f_{44}	12.40118(8)	0.052(3)	-3.09(5)	
f_{45}	1.47036(8)	0.052(3)	1.82(5)	doub2
f_{46}	4.66424(9)	0.051(3)	-3.02(5)	
f_{47}	10.85524(8)	0.050(3)	3.15(5)	
f_{48}	4.20959(8)	0.049(3)	0.48(5)	
f_{49}	8.8136(1)	0.043(3)	-1.25(6)	
f_{50}	2.59328(8)	0.049(3)	0.74(5)	
f_{51}	14.78131(7)	0.054(3)	2.14(5)	doub4
f_{52}	6.43805(9)	0.046(3)	-1.05(5)	
f_{53}	2.67483(8)	0.047(3)	0.79(5)	
f_{54}	12.75445(8)	0.050(3)	1.92(5)	
f_{55}	3.04036(8)	0.047(3)	0.37(5)	
f_{56}	7.01888(9)	0.045(3)	-2.87(6)	trip1
f_{57}	7.71751(9)	0.043(3)	0.68(6)	doub4
f_{58}	8.83337(9)	0.043(3)	1.25(6)	
f_{59}	4.6562(1)	0.044(3)	0.15(6)	
f_{60}	2.00851(9)	0.042(3)	-1.62(6)	doub2
f_{61}	14.0422(1)	0.042(3)	-2.44(6)	
f_{62}	14.74834(9)	0.046(3)	-0.55(5)	trip3
f_{63}	9.9917(1)	0.036(3)	-2.83(7)	
f_{64}	14.4382(1)	0.034(3)	2.47(7)	
f_{65}	9.0918(1)	0.040(3)	2.44(6)	quint2
f_{66}	16.6167(1)	0.035(3)	-1.87(7)	
f_{67}	5.3722(1)	0.035(3)	-0.75(7)	
f_{68}	3.7381(1)	0.035(3)	-2.07(7)	
f_{69}	8.7384(1)	0.033(3)	-1.10(8)	
f_{70}	7.3050(1)	0.031(3)	-0.06(8)	trip2
f_{71}	7.5433(1)	0.032(3)	2.95(8)	doub5
f_{72}	5.5219(1)	0.031(3)	-2.36(8)	
f_{73}	13.9403(1)	0.028(3)	-2.74(9)	
f_{74}	14.0314(2)	0.026(3)	3.0(1)	
f_{75}	6.4843(2)	0.026(3)	-2.4(1)	
f_{76}	14.5770(1)	0.029(3)	2.75(9)	trip3
f_{77}	14.4057(2)	0.018(3)	1.0(1)	trip3
f_{78}	14.9525(2)	0.018(3)	-0.1(1)	doub4

Table E.3. continued.

id.	Frequency (d^{-1})	Amplitude (mmag)	Phase (rad)	Notes
f_{79}	18.5653(2)	0.019(3)	-0.3(1)	